J. Fluid Mech. (2010), *vol.* 648, *pp.* 225–256.
doi:10.1017/S0022112009993053

The wake behind a cylinder rolling on a wall at varying rotation rates

B. E. STEWART[1,2]†, M. C. THOMPSON[1], T. LEWEKE[2] AND K. HOURIGAN[1,3]

[1]Fluids Laboratory for Aeronautical and Industrial Research (FLAIR), Department of Mechanical and Aerospace Engineering, Monash University, Melbourne, Victoria 3800, Australia

[2]Institut de Recherche sur les Phénomènes Hors Equilibre (IRPHE), CNRS/Universités Aix-Marseille, 49 rue Frédéric Joliot-Curie, BP 146, F-13384 Marseille cedex 13, France

[3]Division of Biological Engineering, Monash University, Melbourne, Victoria 3800, Australia

(Received 22 February 2009; revised 26 October 2009; accepted 26 October 2009)

A study investigating the flow around a cylinder rolling or sliding on a wall has been undertaken in two and three dimensions. The cylinder motion is specified from a set of five discrete rotation rates, ranging from prograde through to retrograde rolling. A Reynolds number range of 20–500 is considered. The effects of the nearby wall and the imposed body motion on the wake structure and dominant wake transitions have been determined. Prograde rolling is shown to destabilize the wake flow, while retrograde rotation delays the onset of unsteady flow to Reynolds numbers well above those observed for a cylinder in an unbounded flow.

Two-dimensional simulations show the presence of two recirculation zones in the steady wake, the lengths of which increase approximately linearly with the Reynolds number. Values of the lift and drag coefficient are also reported for the steady flow regime. Results from a linear stability analysis show that the wake initially undergoes a regular bifurcation from a steady two-dimensional flow to a steady three-dimensional wake for all rotation rates. The critical Reynolds number Re_c of transition and the spanwise wavelength of the dominant mode are shown to be highly dependent on, but smoothly varying with, the rotation rate of the cylinder. Varying the rotation from prograde to retrograde rolling acts to increase the value of Re_c and decrease the preferred wavelength. The structure of the fully evolved wake mode is then established through three-dimensional simulations. In fact it is found that at Reynolds numbers only marginally ($\sim$5 %) above critical, the three-dimensional simulations indicate that the saturated state becomes time dependent, although at least initially, this does not result in a significant change to the mode structure. It is only at higher Reynolds numbers that the wake undergoes a transition to vortex shedding.

An analysis of the three-dimensional transition indicates that it is unlikely to be due to a centrifugal instability despite the superficial similarity to the flow over a backward-facing step, for which the transition mechanism has been speculated to be centrifugal. However, the attached elongated recirculation region and distribution of the spanwise perturbation vorticity field, and the similarity of these features with those of the flow through a partially blocked channel, suggest the possibility that the mechanism is elliptic in nature. Some analysis which supports this conjecture is undertaken.

† Email address for correspondence: stewart.bronwyn01@gmail.com

1. Introduction

The flow past a stationary cylinder, placed transverse to a free stream, has been the subject of research for many decades, motivated by wide-ranging relevance to building construction, offshore engineering, aerodynamics and vortex-induced vibration, to name just a few examples. The present investigation examines the flow around a cylinder moving along a wall, with a range of imposed rotation rates. Particular attention is paid to the steady and unsteady structures that develop in the wake. By studying the two- and three-dimensional transitions, it is also possible to determine in what way these flows are altered by the combined effects of translation and rotation when the body is in near contact with a wall. A clearer understanding may then be gained of the fundamental mechanisms that govern the flow.

When the flow around a cylinder in a free stream is steady and separated, the downstream length of the recirculation region has been found to increase linearly with Reynolds number Re (Taneda 1956; Kawaguti 1966; Tamaki & Keller 1969; Dennis & Chang 1970; Fornberg 1985). As these steady recirculation zones grow in length, small convective oscillations of the flow begin in the downstream wake for $30 < Re < 45$ (Taneda 1956). As the Reynolds number is increased, the attached recirculation region becomes absolutely unstable at $Re > 46$ (e.g. Roshko 1954; Jackson 1987; Provansal, Mathis & Boyer 1987; Henderson 1997). The vortex shedding behind the cylinder then takes the form of the Bénard–von Kármán vortex street.

The unsteady two-dimensional wake undergoes a transition to three-dimensional flow at $Re \approx 190$; the form of the instability is described by Williamson (1988) and referred to as mode A. This instability manifests in the formation of pairs of counter-rotating streamwise vortices with a spanwise wavelength of approximately four diameters (Williamson 1996; Henderson 1997; Barkley, Tuckerman & Golubitsky 2000).

When a cylinder in a free stream is subjected to an imposed rotation, several effects become apparent. Not surprisingly, the rotation creates an asymmetry in the wake that becomes more pronounced as the rotation rate increases (Tang & Ingham 1991). This imposed rotation furthermore has a strong influence on the lift and drag forces experienced by the cylinder, as well as having the ability to suppress the unsteady flow. Throughout the present investigation, the non-dimensional rotation rate is given by α and is defined as the ratio of tangential velocity on the surface of the cylinder divided by the free-stream velocity.

At Reynolds numbers $Re \leqslant 60$, investigations of the cylinder in an unbounded flow have shown that imposing a cylinder rotation results in a steady flow which differs significantly from that behind a non-rotating cylinder. Numerical simulations show that the body rotation is able to eliminate one or both of the recirculation zones behind the cylinder, and at higher Reynolds numbers, unsteady flow may be suppressed (Ingham 1983; Tang & Ingham 1991). Jaminet & Van Atta (1969) explained the mechanism for suppression of unsteady flow as the merging on both sides of the vortex street when one side is displaced into the other via the cylinder rotation. This results in suppression of shedding from both sides of the cylinder simultaneously.

As for the case of the non-rotating cylinder, increasing the Reynolds number of the flow results in a transition to unsteady flow behind the rotating cylinder. At small rates of rotation, the shedding takes the form of the Bénard–von Kármán vortex street (Jaminet & Van Atta 1969; Díaz *et al.* 1983; Mittal & Kumar 2003). The asymmetry of the rotational effects results in the shedding and boundary layer

separation tending to favour the side of the cylinder with motion opposing the free stream (i.e. with an imposed flow reversal; Díaz *et al.* 1983). The effect of varying rotation rate on the wake frequency is still not well understood, as experimental studies by Van Atta (1997), Jaminet & Van Atta (1969) and Barnes (2000) found the Strouhal number St to increase steadily with the rotation rate, while the two-dimensional numerical investigation of Mittal & Kumar (2003) found a very slight decrease in St. Furthermore, the results of Kang, Choi & Lee (1999) showed negligible change.

For the Reynolds numbers considered in the present study, the greatest contribution to the lift for the rotating cylinder (for $\alpha \leqslant 1$) is given by the pressure, rather than the frictional (viscous) forces (Tang & Ingham 1991; Chen, Ou & Pearlstein 1993; Kang *et al.* 1999; Mittal & Kumar 2003). However, for the drag force the frictional drag is found to be of the same order of magnitude as the pressure drag. Tang & Ingham (1991) and Kang *et al.* (1999) cited values of the coefficient of lift due to the pressure components as being greater than 90 %. The percentage of this contribution appears to increase with Re.

For $0 < \alpha < 2.5$, Kang *et al.* (1999) found that the pressure and frictional components of the drag change in dominance. At lower magnitudes of rotation, the pressure drag dominates. However, as the rotation increases, this contribution decreases, and at $\alpha \approx 1.5$, the frictional drag provides the greatest contribution to the total drag on the cylinder. Interestingly, in the present study in which the cylinder is rotating near the wall, the frictional drag only dominates over a small range of negative α.

Early studies by Taneda (1965) showed that the presence of a stationary wall near a stationary cylinder acts to stabilize the flow. Steady flow around a wall-mounted obstacle is typified by a single recirculation zone, which has a separation point on the body and a reattachment point on the downstream wall, such as that over a backward-facing step (Armaly *et al.* 1983). In the current study, the plane wall has been given an imposed velocity that eliminates boundary layer effects. Arnal, Goering & Humphrey (1991) found, in their investigation of the flow around a wall-mounted square cylinder, that the introduction of a relative wall velocity creates a second recirculation zone, positioned behind the body, between the primary recirculation zone and the wall. Furthermore, they found that the presence of the wall delays the onset of unsteady flow until higher Re compared with the body in a free stream.

When the cylinder is positioned near (but not in contact with) the moving wall, the fluid passing through the gap is accelerated (Kano & Yagita 2002; Huang & Sung 2007; Nishino, Roberts & Zhang 2007), and Nishino *et al.* (2007) found that the length of the recirculation zone behind the cylinder increases dramatically as the distance between the cylinder and the wall goes to zero.

One significant way in which the wall proximity is able to alter the flow is via the suppression of vortex shedding when the wall distance is below some critical value (Lei, Cheng & Kavanagh 1999). For gap ratios greater than this value, the flow is comparable to that around a cylinder in a free stream. An explanation for this was offered by Nishino *et al.* (2007), who stated that for the cylinder near a moving ground, the nearby wall can have an effect similar to that of a splitter plate in the wake. They proposed that the ground restricts the appearance and growth of disturbances in the wake that can lead to an absolute instability and the onset of Bénard–von Kármán vortex shedding. Rather than the presence of an absolute instability, they observed that the wake displays only convective instabilities as the cylinder nears the wall.

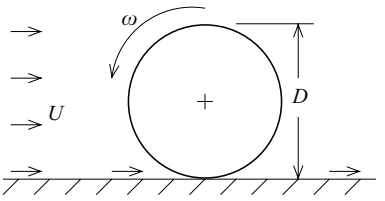

FIGURE 1. A simple schematic of the problem under consideration.

When a square cylinder is placed in contact with the moving wall, Arnal *et al.* (1991) found that the wall encouraged the onset of unsteady flow, compared with the stationary-wall case. Dipankar & Sengupta (2005) stated that the instability arising between the cylinder wake and the wall is due to the interaction of the convecting vortex core shed from the free-stream side of the cylinder. This was first proposed by Sengupta, De & Sarkar (2003), who tested this theory by using a rotating cylinder positioned above the wall to act as a captive vortex. The movement of this 'vortex' was found to create a weak streamwise pressure gradient, which in turn destabilizes the wall shear layer. Furthermore, experiments by Lim, Sengupta & Chattopadhyay (2004) found that the instability effects are enhanced when the vorticity in the wall shear layer and the convecting vortex are of opposite sign. In such cases, the adverse pressure gradient imposed by the convecting vortex will be much larger and will destabilize the downstream wall shear layer. When the vorticity of the two are of the same sign, the disturbance in the flow is much less, and depending on the distance between the vortex and the wall, the shear layer is largely unaffected. The proximity of the wall also results in an increase in the lift force on the non-rotating cylinder (Zdravkovich 1985; Huang & Sung 2007; Nishino *et al.* 2007).

2. Problem description and methodology

The problem set-up considered in the present investigation is that of a cylinder moving along a plane wall through a quiescent fluid. The motion of the cylinder may be rolling or sliding, or a combination of the two; both positive (prograde) and negative (retrograde) rotation rates are considered. Using a frame of reference attached to the cylinder simplifies the computational analysis. In this frame, the cylinder remains fixed, with the fluid and the wall moving past the cylinder as shown in figure 1. Here, D is the diameter of the cylinder and U the translational velocity, and the angular velocity is denoted ω.

The relative motion of the body and the fluid allows this problem to be characterized in terms of two parameters: the Reynolds number and the non-dimensionalized rotation rate of the cylinder. The Reynolds number is defined by $Re = \rho U D/\mu$, where μ is the coefficient of dynamic viscosity and ρ is the fluid density. A range of $20 < Re < 500$ is considered in order to capture the two- and three-dimensional transitions in the flow. For the frame of reference attached to the cylinder centre, the body rotation can be defined by the ratio of the rotational to the free-stream velocity. This is given by $\alpha = D\omega/2U$, where positive α has the anticlockwise sense of rotation (prograde) indicated in figure 1. When $\alpha = 1$, the body moves in the intuitive sense of forward rolling. This corresponds to the case of the body and the plane wall moving at the same relative velocity, at their nearest points, without slipping. The term 'retrograde rolling' will be used to describe the case in which $\alpha < 0$, and $\alpha = -1$ corresponds to the case in which the nearest points of the body surface and the wall

are moving at equal magnitudes but in opposite directions. During this investigation, attention is given to five discrete values of the rotation rate. These are $\alpha = 1$, 0.5, 0, -0.5 and -1.

Values of the lift and drag coefficients, and the Strouhal number, are also reported. The lift and drag coefficients are calculated from the total force acting on the cylinder surface and are given by $C_L = F_L/\rho U^2 R$ and $C_D = F_D/\rho U^2 R$, respectively. Here, R is the radius of the cylinder and F_L and F_D are the lift and drag forces. In the unsteady wake regimes, the Strouhal number is calculated according to $St = f_s D/U$, where f_s is the frequency of vortex shedding associated with the unsteady wake.

In order to prevent a singularity arising in the numerical simulations from the collapse of the elements directly underneath the cylinder, it is necessary to impose a small displacement G between the cylinder and the wall. Throughout this investigation, the gap ratio, defined as G/D, is set equal to 0.005. The choice of this value, along with a sensitivity study, shall be discussed in the following sections.

2.1. *Numerical scheme*

As indicated above, simulations are carried out in the non-rotating frame attached to the cylinder centre, and all results are presented with the flow moving from left to right. As the frame of reference is not accelerating, no additional terms need to be included in the governing equations. Instead, the influence of the moving frame is effected through modifications to the boundary conditions. For simplicity, the results are represented in the non-dimensional form, with the relevant variables normalized by the body diameter and the free-stream velocity. Likewise, the time t is non-dimensionalized according to $\tau = tU/D$.

The numerical scheme solves the viscous, incompressible Navier–Stokes equations. These comprise the equations governing momentum transport,

$$\frac{\partial \boldsymbol{u}}{\partial t} = -(\boldsymbol{u}\cdot\nabla)\boldsymbol{u} - \frac{1}{\rho}\nabla P + \frac{1}{\rho}\nabla\cdot\mu\nabla\boldsymbol{u} \tag{2.1}$$

and continuity,

$$\nabla\cdot\boldsymbol{u} = 0, \tag{2.2}$$

where $\boldsymbol{u}(x, y, z, t) = (u, v, w)$ is the velocity vector, ρ the fluid density, P the scalar pressure field and μ the dynamic viscosity.

Equations (2.1) and (2.2) are discretized with the use of a semi-implicit spectral-element scheme that incorporates time-splitting for the temporal discretization. This code has previously been used to obtain accurate solutions for the flow around cylinders (Thompson, Leweke & Williamson 2001*b*; Ryan, Thompson & Hourigan 2005), spheres (Thompson, Leweke & Provansal 2001*a*; Thompson *et al.* 2006) and rings (Sheard, Thompson & Hourigan 2003). Temporal discretization takes place via a fractional step method (Chorin 1968). The implementation for the spectral-element method is given in Karniadakis, Israeli & Orszag (1991).

Dirichlet boundary conditions are used to specify the velocity at the inlet and transverse boundaries and on the cylinder surface. For $\alpha = 0$, when the cylinder is not rotating, a no-slip condition is defined at the body surface. The lower boundary, which is positioned just below the body, has a specified velocity equal to the free-stream flow. The upper boundary also has an imposed velocity equal to that of the free stream, which is acceptable provided this boundary is positioned very far from the body. The downstream boundary is defined in terms of a von Neumann condition for the velocity. Three-dimensional computations were performed by using a Fourier

expansion in the spanwise direction. Further information on the implementation is given in the references cited above.

2.2. *Linear stability analysis*

In order to examine the sensitivity of the flow around the cylinder to three-dimensional perturbations in the spanwise direction, a linear stability analysis is carried out. This involves solving the linearized Navier–Stokes equations based on a pre-computed two-dimensional base flow. The approach has been documented in, for example, Ryan *et al.* (2005).

This procedure results in a set of equations governing the perturbation field, the exponential growth or decay of which can then be monitored over time. As the resulting partial differential equations are linear and have constant coefficients with respect to the spanwise coordinate z, the functional dependence on this variable can be expressed as a sum of complex exponential terms of a Fourier expansion, with each term corresponding to a different spanwise wavelength λ, treated separately.

Linear stability theory then considers solutions of the form

$$\hat{r}(x, y, t + T) = \hat{r}(x, y, t) \exp \sigma T, \tag{2.3}$$

where $\hat{r}$ is a complex amplitude coefficient of any of the spanwise perturbation fields for the pressure or velocity components and T is a relevant period of time. This form is useful for either a steady or an unsteady base flow. When a steady base flow is considered, T represents an arbitrary period over which the growth of the mode is recorded, and this is typically of the order of one non-dimensional time unit. In such cases, the stability of the flow is generally referred to in terms of the growth rate σ of the mode.

In practice, the complex eigenvalue problem does not need to be set up and solved explicitly. The dominant modes can be found by integrating in time from a white noise perturbation and extracting the modes and growth rates using an Arnoldi decomposition as done by Barkley & Henderson (1996).

For a specified λ, the Reynolds number at which the growth rate equals zero is termed the critical Reynolds number. This indicates the value above which the flow will become locally unstable to three-dimensional perturbations and below which the flow will remain two-dimensional. Further details of this method are given in Leontini, Thompson & Hourigan (2007) and Griffith *et al.* (2007). Although the method has been implemented to calculate the first few eigenvalues using a Krylov-based approach (e.g. Barkley & Henderson 1996), for the results reported in the current paper only the dominant eigenmode is presented.

2.3. *Resolution studies*

The mesh used for the two-dimensional study is shown in figure 2, with increased resolution present in the vicinity of the cylinder and to capture the small-scale structures in the wake. This increased resolution is maintained for a distance of $30D$ downstream of the cylinder. Immediately beneath the cylinder, the domain is spanned by two macro-elements. This means that typically there are 15 node points (for $N = 8$, see the discussion below) between the cylinder and the wall. For negative values of α, the flow remains stable over a range of Re wider than that for $\alpha > 0$. Resolution studies were therefore undertaken for the extreme values of the rotation rate, $\alpha = -1$ and 1, and the Reynolds number, $Re = 20$, 200 (for $\alpha > 0$) and 500 (for $\alpha < 0$). For the unsteady flow regime, the wake is considered to have reached the converged periodic solution when the variation in the peak lift is less than 1 % over several cycles (which

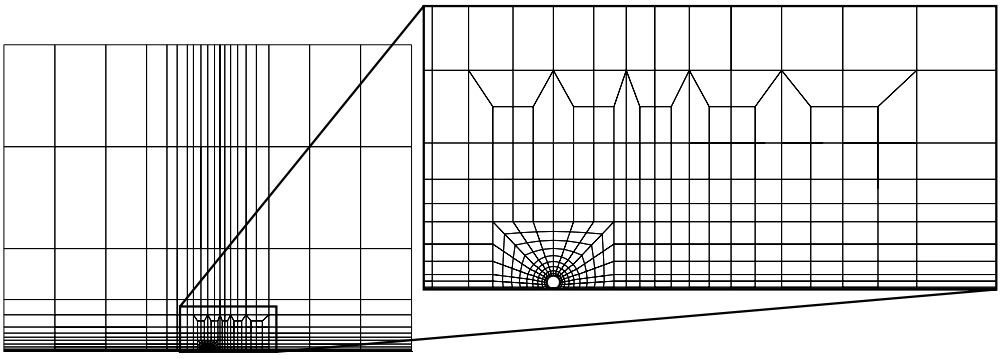

FIGURE 2. View of the cylinder macro-element mesh with detail of the region near the body.

in the majority of cases was less than 0.1 %). The Strouhal number is then calculated from the frequency of the fluctuating lift coefficient.

The numerical code was tested to ensure that the solution is insensitive to variations in the chosen time step Δt. This is indeed found to be the case, and halving the time step from 0.001 to 0.0005, for the Re and α given above, shows a variation in C_L, C_D and St of less than 0.1 %.

The streamwise and transverse boundaries are placed far from the cylinder location to reduce blockage effects. Three different meshes were used to investigate blockage. The position of the upstream and downstream boundaries are given by $x1$ and $x2$, respectively, while the position of the transverse boundary is given by $y1$. All boundary positions are non-dimensional and are given in terms of the cylinder diameter, D. The three meshes, C1, C2 and C3, had the dimensions $(x1, x2, y1) = (75, 75, 100)$, $(100, 100, 150)$ and $(150, 150, 200)$, respectively. The variation in C_L, C_D and St between the two finest meshes was at most 0.1 %; hence the intermediate mesh, C2, was used for the remainder of the study.

When using the spectral-element method, Lagrange interpolants of order $N-1$ are used to represent the solution variables during the spatial discretization, where N is the number of interpolation points in each direction. As part of the resolution study, the number of the N $(\times N)$ internal node points within each macro-element of the mesh was varied from 6 to 10. The study indicated that for $N \geqslant 7$ the force and Strouhal number predictions were converged to better than 0.1 %. Therefore, $N = 8$ provides stable, converged solutions and is used throughout the remainder of the simulations. During the stability analysis, the peak growth rate at the critical Reynolds number was also found to be insensitive to increases in the polynomial order, with no change in σ as N is increased from 8 to 9.

As mentioned previously, it was necessary to impose a small gap between the body and the wall to avoid a collapsed mesh element at the wall. The gap was minimized as far as possible to accurately model the flow around a cylinder positioned in contact with the wall. Towards this end, seven separate meshes were constructed with gap ratios ranging from 0.004 to 0.01, with $G/D = 0.004$ being the minimum value as imposed by the stability of the numerical scheme. Over this range of gap ratios, the variation of the key parameters at the high- and low-Re limits is tested.

The variations of the lift and drag coefficients at $Re = 20$ and $Re = 50$ and 200 are shown in figure 3 and 4, respectively. The lift shows a slight increase as the gap ratio is reduced for all values of α, and the trend is approximately linear. The drag coefficient in figure 3 shows a clearly nonlinear relationship and increases according

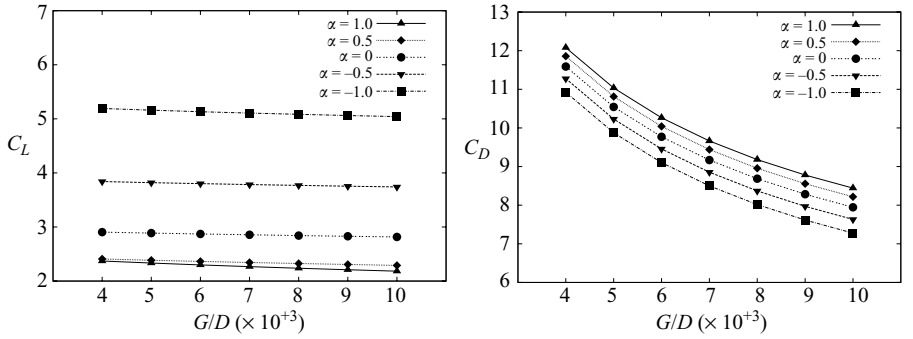

FIGURE 3. Variation in the lift and drag forces with varying gap ratio at $Re = 20$.

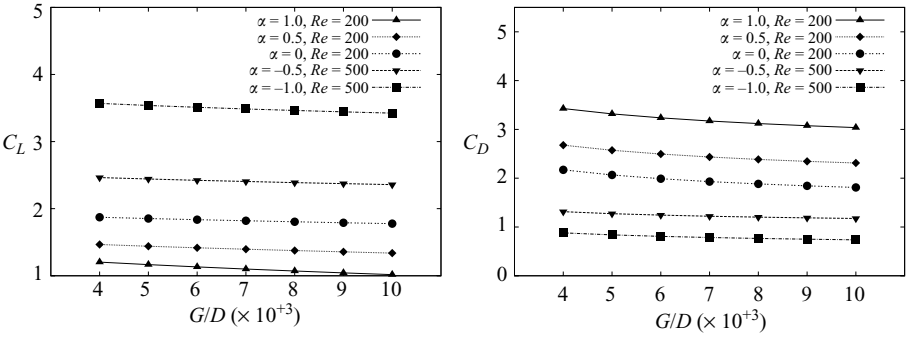

FIGURE 4. Variation in the lift and drag forces with varying gap ratio at $Re = 200$ and 500.

to a power law as $G/D \to 0$. This increase in C_D is due to a substantial increase in the pressure force as the flow through the small gap is suppressed. The drag data are well approximated by a curve of the form $C_D = a(G/D)^b$, where $a \approx 1.2$ and $b \approx -0.41$.

While there is some variation in the force coefficients for smaller Reynolds numbers as the gap ratio is reduced (associated with the sensitivity of the pressure beneath the cylinder to gap size), streamline plots for different G/D show no discernible difference away from the immediate vicinity of the gap. The predicted flow structures are assumed to be general, applicable to the zero-gap case, except in the immediate vicinity of the lowest point on the cylinder. For the unsteady cases, the Strouhal number was found to vary linearly with the gap ratio. The greatest effect was at the highest rotation rates. In the worst case, the Strouhal number is still predicted to be within 2 % of the (extrapolated) zero-gap-ratio value. All simulations from this point forward are presented with the mesh of gap ratio 0.005.

The topological wake structure from three-dimensional simulations are compared with the predicted instability modes determined using the linear stability analysis. To carry out the three-dimensional simulations, the two-dimensional mesh is expanded in the spanwise direction using 36 Fourier planes, spanning either one wavelength or four wavelengths of the dominant linear three-dimensional instability mode for each rotation rate. Mesh C2 is also used for all three-dimensional simulations, and fifth-order polynomials ($N = 6$) are employed.

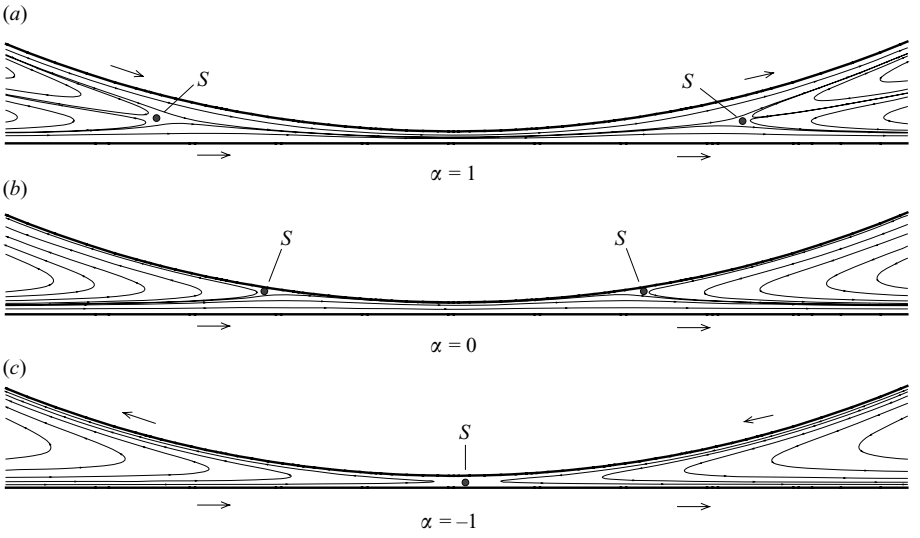

FIGURE 5. Flow through the contact region. Streamlines are plotted for irregularly spaced values of the streamfunction to indicate the location of stagnation points for $Re = 50$. The arrows indicate the relative motion of the cylinder and wall, and the position of stagnation points in the flow are indicated with 'S'.

3. Results

3.1. *Flow in the contact region*

To understand fully the flow structures that form around the rolling cylinder, it is helpful to first examine the flow at the point of near contact between the cylinder and the wall. For any given α, the flow structures are largely insensitive to small changes in the gap ratio; however, the flow is heavily dependent on the value of α chosen. Figure 5 shows streamline plots of the flow in the contact region at representative values of α. Streamlines are plotted at irregular intervals so as to illustrate better the regions in which stagnation points are present. As was observed by Bearman & Zdravkovich (1978) for a cylinder placed near a stationary wall, there exist stagnation points in the contact regions, the number and location of which depend on the value of α. It is not possible to detect any movement of these stagnation points at a given α, either with variations in Re or with the onset of unsteady flow.

Figure 5(*a*) shows the streamlines present for 'normal' (prograde) rolling when $\alpha = 1$. Two stagnation points are present, upstream and downstream of the gap. These are pushed away from the solid boundaries by the entrained fluid layers moving along the wall and the cylinder surface. On the upstream side of the cylinder, the fluid is being carried into the contact region by the moving boundaries. The rapid constriction then causes the flow to change direction, and an outflow jet is formed. The reverse is true on the downstream side of the cylinder, where the boundary motion transports the fluid away from the constriction. The flow on the downstream side of the cylinder is therefore carried into the contact region by a central inflow jet. The stagnation points are present in the regions of hyperbolic flow, as indicated by the streamlines plotted in the frame of reference attached to the cylinder centre. At the point of nearest contact between the cylinder and the wall, the streamlines are almost parallel, and the flow is from left to right.

(*a*) $\alpha = 1$, $Re = 60$. (*b*) $\alpha = -1$, $Re = 300$.

FIGURE 6. Vorticity contours for the steady flow around the cylinder. The streamlines showing the presence of the two recirculation zones are overlaid in black. The streamlines are shown in the frame of reference attached to the cylinder centre.

For $\alpha = 0$ (figure 5*b*), there exist two stagnation points, as for $\alpha = 1$, but these are now positioned on the stationary cylinder surface. The flow is encouraged to pass through the narrow gap by the relative motion of the moving lower wall. The outflow of fluid from the gap on the upstream side and the inflow on the downstream side now take place closer to the cylinder surface rather than in the region equidistant between the two walls. There also exists a very large shear rate near the cylinder surface where the fluid velocity goes to zero.

Figure 5(*c*) shows the representative streamlines for retrograde rotation at $\alpha = -1$. In this case, the motion of the cylinder and the wall are opposite in direction at the point of near contact, creating a single region of hyperbolic flow and a single stagnation point. In this configuration, the fluid on the upstream side of the cylinder is pulled into the gap region along the plane wall before undergoing a reversal and moving away in the direction of cylinder motion. The opposite is true on the downstream side of the cylinder, with the flow leaving the gap region adjacent to the plane wall. From these plots, one would intuitively expect the retrograde case of $\alpha = -1$ to yield the most stable flows, i.e. resisting shedding as the Reynolds number is increased, with the possibility of the incoming flow remaining fully attached as it passes from the upstream wall to the cylinder surface and is then carried downstream with the motion of the plane wall.

The presence of the single stagnation point for $\alpha = -1$ yields a flow analogous to that described by Seddon & Mullin (2006) and which is observed when a continuous row of cavitation bubbles form in the contact region between the cylinder and the wall. These bubbles block the bulk flow through the gap, causing a complete reversal of the flow upstream of the cylinder, and induce a reversed rotation ($\alpha < 0$).

3.2. *Steady flow*

The steady flow over steps and wall-mounted obstacles has been the subject of studies for some time, with recirculation zones frequently observed in the downstream flow. When the obstacle and the downstream wall have zero relative velocity, the flow separating from the trailing edge reattaches to the wall, thereby defining the boundary of a single recirculation zone. In the current investigation, such a reattachment is not possible, as the downstream wall is moving relative to the cylinder. Results from Arnal *et al.* (1991), for the flow behind the square cylinder sliding along a wall, show that this configuration can lead to the formation of 'two' recirculation zones. In the present study, this was also found to be the case, and the order in which these two recirculation zones form is dependent on the rotation rate. Examples of the steady flow vorticity and regions of recirculating fluid for the two extreme rotation rates can be seen in figure 6, when both the upper and lower recirculation zones are present. The closed streamlines (shown as black curves) are plotted in the frame of reference attached to the cylinder and show the location of the upper and lower recirculation zones.

α	1	0.5	0	−0.5	−1
Re_{up}	< 20	<20	<20	70	140
Re_{low}	40	50	70	100	115

TABLE 1. Reynolds number of formation of the upper and lower recirculation zones. *Re* is varied in increments of 5.

When $\alpha = 0.5$ and 1, the rotation of the cylinder entrains a layer of fluid that opposes the free-stream flow. This opposing fluid motion results in an upper recirculation zone, which forms around the cylinder and is displaced away from the wall at its downstream end. When $\alpha = 0$, there is no imposed velocity on the surface of the cylinder, and the upper recirculation zone forms from separation and reattachment points on the cylinder surface. For all rotation rates with $\alpha \geqslant 0$, increasing the Reynolds number leads to the development of a secondary recirculation zone located between the upper recirculation zone and the wall.

The flow around the cylinder for negative rotation rates is topologically similar (except in the vicinity of the cylinder) but is markedly different in the size of the flow structures from that for $\alpha > 0$. Because of the sense of rotation of the cylinder when $\alpha < 0$, the entrained fluid moving with the cylinder surface displaces the recirculation zones away from the boundary and downstream of the cylinder. Also at these rotation rates, the upper recirculation zone is greatly reduced in size, and the lower recirculation zone forms further upstream towards the cylinder than for $\alpha \geqslant 0$.

The upper recirculation zone is present at all Reynolds numbers considered (down to $Re = 20$), for $\alpha = 0.5$ and 1. The steady wake for $\alpha = 0$ (not shown) bears similarities to that for $\alpha = 1$, and again, the upper recirculation zone is present at the lowest Reynolds number considered, $Re = 20$. When retrograde rotation is present, the streamlines of figure 6 show that the reversal of the flow takes place nearer the plane wall, and the majority of the vorticity lies in this region. Unlike the other four values of α studied, the lower recirculation zone forms first for $\alpha = -1$. With the cylinder undergoing retrograde rotation, it is possible for the flow to remain fully attached as it moves with the boundaries. For both $\alpha = -0.5$ and -1, there are no closed recirculation zones present at $Re = 20$. Furthermore, $\alpha = -1$ provides the most stable configuration observed, with steady flow predicted at Reynolds numbers over 300.

The effect of the rotation rate appears to be that positive values of α lead to the displacement of the steady recirculation zone further from the wall, in agreement with the findings of Cheng & Luo (2007), while the negative rotations result in the confinement of the vorticity to the region close to the wall. The vorticity forming over the top of the cylinder is opposite in sign to that generated along the plane wall, and the stability of the flow is enhanced (against two-dimensional shedding) as the rotation rate is varied from 1 to -1.

The formation of the closed recirculation zones is determined by a detailed inspection of the streamlines at each *Re*. The values of the Reynolds number at which the upper and lower recirculation zones are first observed are summarized in table 1. To identify the critical Reynolds number in each case, the simulations are run with *Re* increments of 5, and the simulations are started from an unperturbed flow and are allowed to develop.

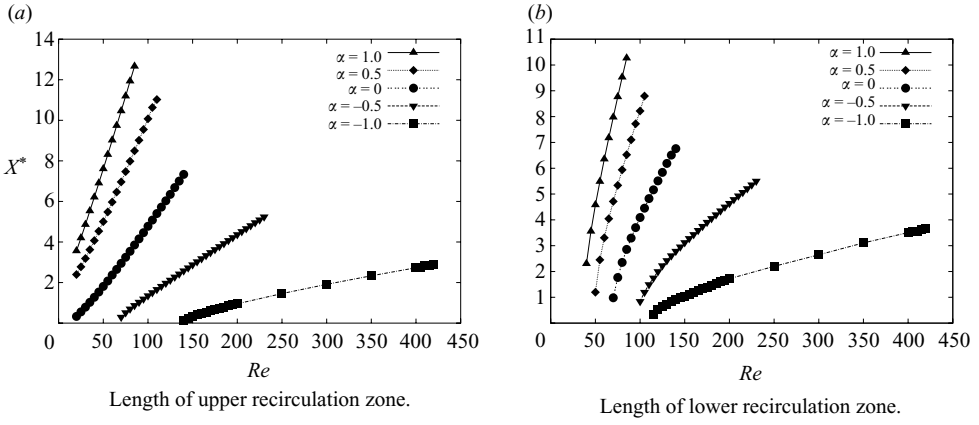

FIGURE 7. Total lengths of the upper and lower recirculation zones.

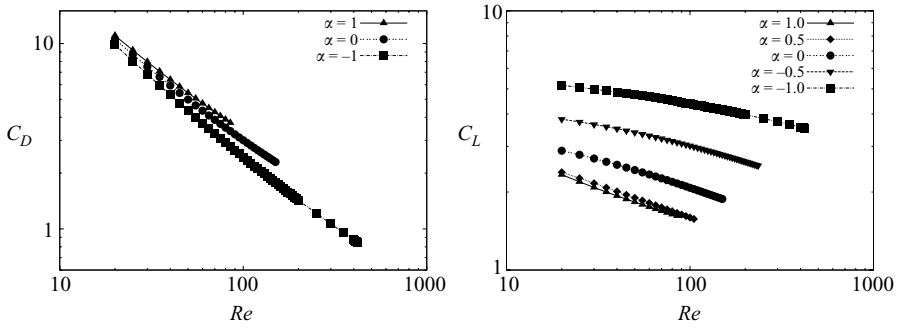

FIGURE 8. Coefficients of drag and lift for varying Re and α in the steady regime.

3.3. *Recirculation lengths*

The position and length of the closed recirculation regions vary with the Reynolds number of the flow. The start and end positions of these zones are measured as the upstream- and downstream-most points of the limiting streamline. Accordingly, for $\alpha > 0$, the start of the upper recirculation zone is upstream of the cylinder, while for $\alpha = 0$, it lies on the downstream cylinder surface, and for $\alpha < 0$, it is located in the wake. The lower recirculation zone terminates at a hyperbolic point in the flow. The overall length of the recirculation zones are shown, for all five rotation rates, in figure 7. The non-dimensional lengths of the two regions are given by $X^* = x/D$, where x is the streamwise coordinate measured from the cylinder centre.

For both the upper and lower recirculation zones, the overall length increases linearly with Re, following an initial period of nonlinear growth at Re just above formation. Such a linear increase in the recirculation length with the Reynolds number is similar to that observed for the recirculation zone behind a cylinder in unbounded flow (Taneda 1956; Kawaguti 1966; Tamaki & Keller 1969; Dennis & Chang 1970; Fornberg 1985).

3.4. *Steady lift and drag trends*

Trends in the lift and drag coefficients have been plotted in figure 8, for the steady flow regime. Although the forces on the cylinder show some sensitivity to the gap ratio, the resolution study described in § 2.3 indicates that the trends shown with

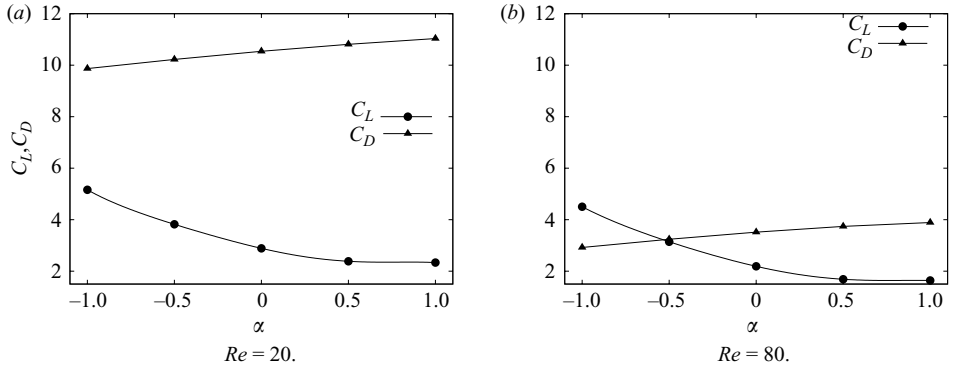

FIGURE 9. Change in C_L and C_D with varying α and fixed Re. Increasing the Reynolds number causes a dramatic decrease in C_D, while the overall trends for C_L and C_D remain largely unchanged.

increasing Re are expected to hold for $G/D \neq 0.005$ when the cylinder is very close to the wall. The coefficient of drag in figure 8 has a log–log relationship that is inversely proportional to Re. Furthermore, the drag coefficient decreases slightly with decreasing α but is only weakly dependent on the rotation rate. For clarity, only the values of $\alpha = -1, 0$ and 1 have been plotted for C_D, with the other rotation rates lying between these curves.

In the case of the non-rotating cylinder away from the wall, Henderson (1997) found that at $Re = 40$, $C_D \approx 1.55$. This is in contrast with the present results for the cylinder sliding along the wall (with $\alpha = 0$), for which the drag coefficient is over three times this value at $C_D = 5.93$. The results of Mittal & Kumar (2003) for the rotating cylinder in an unbounded flow at $Re = 200$ found the values of the mean drag coefficient $\bar{C_D}$ to be approximately 1.05 and 1.27 for $\alpha = \pm 1$ and ± 0.5, respectively. When these values are compared with the present cases in which the cylinder motion assists the fluid flow over the surface ($\alpha = -1$ and $\alpha = -0.5$), the present values of 1.43 and 1.69 again show an increase. These comparisons indicate that while the wall may delay the onset of unsteady flow, the mean drag force experienced by the cylinder increases following the introduction of a nearby wall. This effect becomes pronounced as α varies from -1 to 1.

The effect of changing the rotation rate has a much greater influence on the lift than on the drag, especially when $\alpha < 0.5$. The lift force in figure 8 decreases with increasing Re, and when plotted on log–log axes, the data curves are not as clearly linear as for C_D. When $\alpha = 0.5$ and 1, C_L appears less affected by the varying rotation, and the change in C_L with Re is much closer to a log–log relationship. Unlike the drag force, C_L is observed to increase as α varies from 1 to -1.

The effect of varying the rotation rate in the present study can be seen more clearly in the lift and drag plots of figure 9. As α is varied from -1 to 1, the change in the steady-state lift and drag coefficients is shown at two different Reynolds numbers. At $Re = 20$ (figure 9*a*), the drag force dominates for all α and is approximately two to five times the magnitude of the lift, depending on the value of α. At $Re = 80$ (figure 9*b*), this situation changes, and the lift and drag are of similar magnitude. Furthermore, as the rotation rate is varied from -1 to 1, the forces on the cylinder change from being lift dominated to being drag dominated. For all values of α and Re, the lift force is directed away from the wall. As the Reynolds number is increased beyond

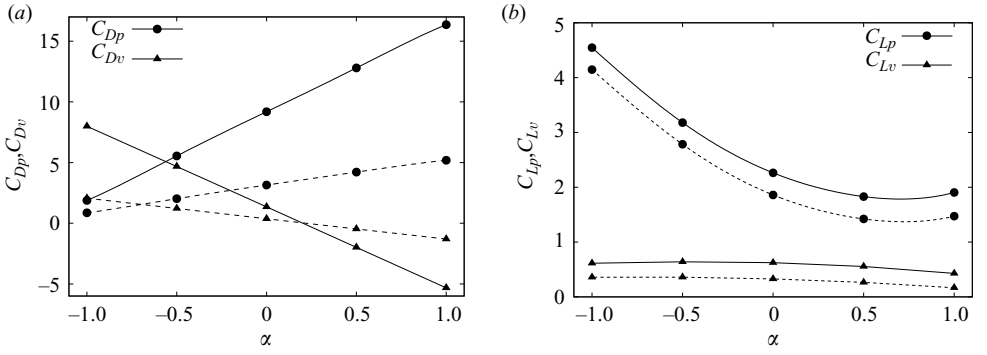

FIGURE 10. Magnitude of the pressure and viscous components of the (*a*) drag and (*b*) lift coefficients for $Re = 20$ (solid lines) and 80 (dashed lines).

$Re = 80$, the flow becomes time dependent for certain values of α, and therefore a direct comparison of the steady flow C_L and C_D cannot be made at higher Re.

The results of figure 9(*b*) show a trend in the lift and drag coefficients that is very similar to those observed by Cheng & Luo (2007), who investigated the flow around a rotating cylinder near a stationary wall at $Re = 200$. They found that at the smallest gap ratios studied ($0.2 < G/D < 0.3$), the flow was steady for all rotation rates. As for the present study at $Re = 80$, the system studied by Cheng & Luo (2007) underwent a transition from lift to drag dominated at $\alpha \approx -0.5$.

The viscous and pressure components of the lift and drag are shown in figure 10 for $Re = 20$ and 80. The viscous component of the drag is dominated by the very large velocity gradients at the cylinder surface near the gap region and varies linearly from positive values at $\alpha = -1$ to negative values at $\alpha = 1$. When the cylinder is undergoing prograde rolling ($\alpha > 0$), the velocity gradients in this region are negative, resulting in a negative viscous drag. A decrease in the viscous drag is offset by an increase in the pressure drag as α varies from -1 to 1. The result is that the total drag force is only slightly affected by varying the rotation rate, while the magnitudes of the pressure and viscous components decrease with increasing Re.

Relative contributions of the pressure and viscous forces on the lift remain almost constant for a given α and increasing Re throughout the steady regime. Figure 10 shows the relative contributions at $Re = 20$ and 80. In both cases, the viscous component of the lift remains fairly constant with changing α, while the pressure force provides the dominant contribution to the lift force and decreases as α varies from -1 to 1. A slight increase in C_{Lp} is observed for $0.5 < \alpha < 1$, with $\alpha = 1$ having a higher value of C_{Lp}. This increase in the pressure component results in the total lift coefficient being almost equal for $\alpha = 0.5$ and 1. This is in contrast with the results of Cheng & Luo (2007), who found C_L to decrease steadily with the rotation rate for $Re = 200$. This may be due to the larger gap ratios employed in their study and/or the fact that the plane wall was stationary.

The drag coefficient is dominated by the pressure force for all $\alpha \neq -1$. The current observations of the lift force being dominated by the pressure and switching of dominance between the pressure and viscous drag are in agreement with the observations by Kang *et al.* (1999), Tang & Ingham (1991) and Mittal & Kumar (2003) for the rotating cylinder in a free stream. However, in this instance the contribution of C_{Lv} to the total lift is far more significant than for those cases in which the wall is not present.

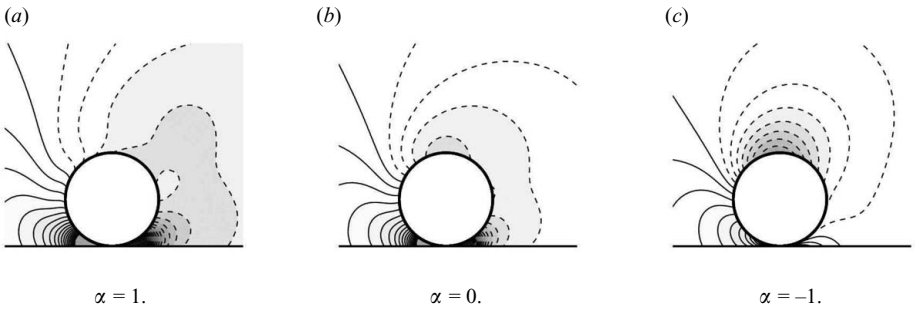

FIGURE 11. Contours of constant pressure around the cylinder at $Re = 20$ and various rotation rates. The regions of negative pressure are enclosed with the dashed lines.

The large change in the drag coefficient and the relative invariance of the lift coefficient with the Reynolds number are presumably due to the significant change in size of the wake region, leading to a change in the base pressure, and the modification of the boundary layer width at the top of the cylinder, both of which will primarily affect the drag coefficient.

The dominant pressure forces in the system occur in the gap region beneath the cylinder. A positive peak in the pressure develops upstream of the gap where there is strong converging flow, and a negative pressure develops downstream in the diverging region. The magnitude of these pressures increases greatly for the cylinder undergoing positive rotation. The magnitude of the pressure forces are greater at lower Reynolds numbers, and as Re increases in the steady regime, the magnitude of these pressures steadily decreases for all α.

Figure 11 shows the contours of constant pressure in the region of the cylinder for the steady flow regime. Results are shown for representative values of α, with negative pressures enclosed by the dashed lines. Varying the rotation rate from forward to reversed rolling causes a region of low pressure to move from the rear of the cylinder towards the top of the body, away from the wall. For $\alpha = -1$ (figure 11*c*), the region of negative pressure is concentrated near the top of the cylinder, resulting in an increase in the total lift force. However, it can be seen that the low pressures on the cylinder surface still extend around the downstream side of the cylinder and into the gap region.

4. Unsteady flow

4.1. *Critical Re of transition*

The critical Reynolds numbers at which the two-dimensional simulations first become unsteady are given in figure 12 and table 2. It has previously been found that the presence of the wall is able to suppress unsteady flow as the gap ratio is reduced, and the critical Reynolds number of transition may be extended well beyond that for a cylinder in a free stream (Arnal *et al.* 1991; Cheng & Luo 2007; Nishino *et al.* 2007). In the present study, for $\alpha = 0$, the critical Reynolds number is found to be $Re \approx 160$. This is 3.5 times greater than the value of Re observed for a cylinder in unbounded flow.

From the results of Cheng & Luo (2007), it was found that for the rotating cylinder near the stationary wall, the flow is steady for all $-1 < \alpha < 1$ at gap ratios of 0.2–0.3 and $Re = 200$. As the gap ratio in the present study is well below these values, and

α	1	0.5	0	−0.5	−1
Re_c	35.6	48.2	70.8	112	182
λ_c/D	8.5	6.9	5.4	3.6	2.2
Re_{c2d}	90	115	160	245	425

TABLE 2. Critical wavelength and Reynolds number at which the three-dimensional mode first develops. Also shown are the transition Reynolds numbers for two-dimensional steady to two-dimensional unsteady flow.

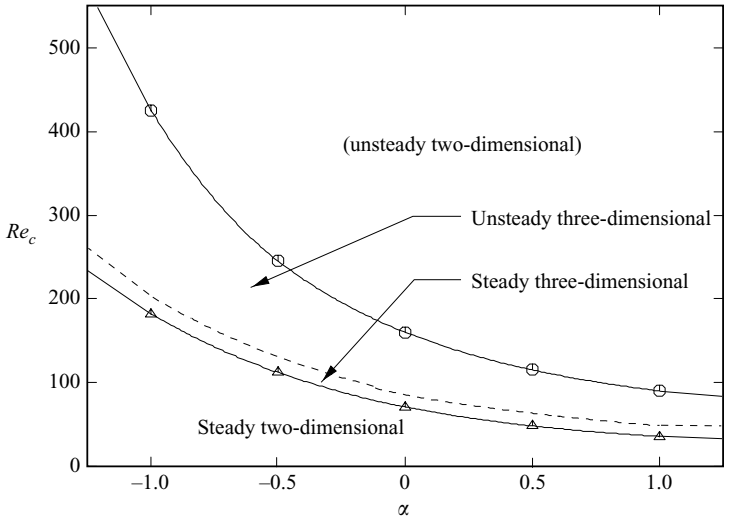

FIGURE 12. Transition map showing the critical Reynolds numbers for two-dimensional steady → two-dimensional unsteady, two-dimensional steady → three-dimensional steady and three-dimensional steady → three-dimensional unsteady transitions. Details are provided in the text.

the transition to unsteady flow occurs at $Re < 200$ for several values of α, the results indicate that the relative motion of the plane wall has a significant destabilizing effect on the flow when compared with the cylinder positioned near a stationary wall.

4.2. *Flow structures*

When the flow becomes time dependent, vortex shedding takes place in the cylinder wake. The shear-layer vorticity that forms over the top of the cylinder rolls up into a strong, compact vortical structure. This in turn destabilizes the wall shear layer as described in the studies of Sengupta *et al.* (2003) and Lim *et al.* (2004). The current flow satisfies the criteria laid out by Lim *et al.* (2004) for unsteady flow to occur, namely that the shed vortex is moving significantly slower than the free stream and that the vorticity in the wall shear layer and the shed vortex are of opposite sign.

The destabilized wall shear layer rolls up and forms a counter-rotating vortex pair with the shed vortex. A similar phenomenon has been observed by Arnal *et al.* (1991), in the wake behind a square cylinder in contact with and translating along a plane wall. The movement of the shed vortices in the present study is shown in figure 13, at $Re = 200$ and $\alpha = 0$, over a typical shedding cycle. The unequal strength of the two

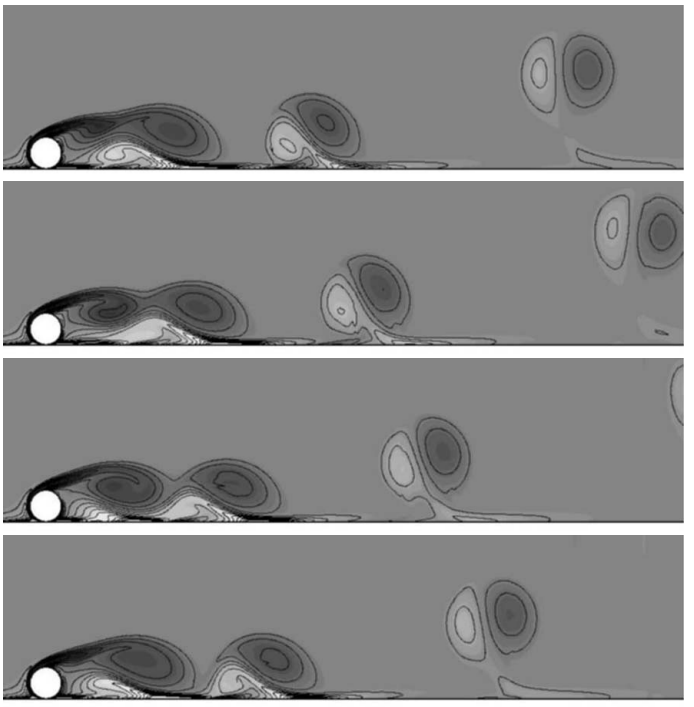

FIGURE 13. Vorticity contours for the cylinder with $\alpha = 0$ at $Re = 200$ over a single shedding cycle. Negative vorticity forming over the top of the cylinder is shown by the black contours, and positive vorticity near the wall is shown in grey. Time increases from top to bottom in steps of one quarter of a period.

vortices results in a net clockwise rotation of the weaker vortex around the strongest vortex as they propel away from the wall. Following this series of images in figure 13, the shedding sequence repeats from the top.

Figure 14 shows a comparison of the vortex shedding for various cylinder rotation rates. All images are shown at the moment of maximum lift in the shedding cycle. The plots on the left give the vorticity contours at $Re = 200$ for the values of $\alpha \geqslant 0$. From this, it is apparent that increasing the rotation rate from 0 to 1 decreases the formation length of the flow and increases the circulation of the vortices, causing the vortex pair to migrate further from the wall. There is also an associated drop in the shedding frequency, which will be discussed in more detail later. At $Re = 200$, the simulations with negative rotation rates exhibit steady flow. It is therefore necessary to consider higher-Reynolds-number flows when $\alpha < 0$. The plots on the right show the unsteady flows for $\alpha \leqslant 0$ when $Re = 450$. At this higher Re, the flow for $\alpha = 0$ now closely resembles the flow with $\alpha = 1$ from figure 14. Increasing the Reynolds number therefore has a similar effect on the flow as increasing the rotation rate. The wake for $\alpha = -1$ is markedly different from the other cases, as the frequency of shedding is much higher, and the weak vortex pairs remain adjacent to the wall as they move downstream. This is presumably related to the fact that for $\alpha = -1$, the velocity at the top of the cylinder matches the free-stream velocity. While there will still be some speed-up of the flow as it passes over the cylinder, the rate at which vorticity is shed into the wake will be greatly reduced.

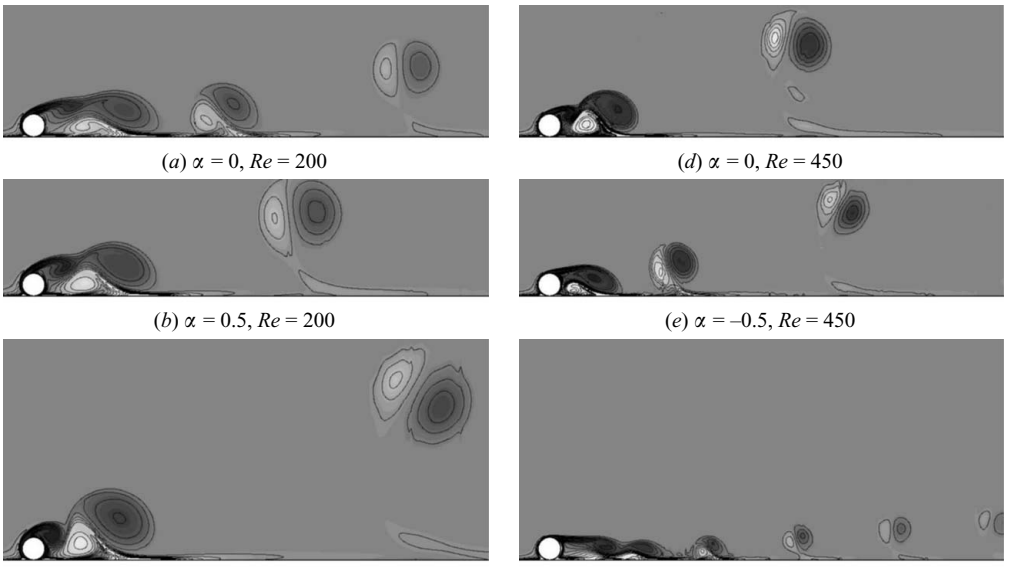

FIGURE 14. Vorticity contours for unsteady shedding for a selection of rotation rates. The left column shows the results for $Re = 200$ and the right column for $Re = 450$. The contours of vorticity are as in figure 13.

4.3. *Comparison with experiments*

In addition to numerical simulations, experiments were also performed as part of this research programme. The experimental rig has been fully described in Stewart *et al.* (2008, forthcoming) in a study on the flow past a sphere, and in order to save space and because it is not the main focus of the present study, it will not be described here, except to mention a few salient features. The experiment required a moving floor. This was implemented using a driven, tensioned flexible belt passing over rollers at each end of the working section. Upstream of the moving floor, the boundary layer was removed by suction, allowing a uniform flow on to the motor-driven cylinder. Flow visualization was performed using careful upstream injection of fluorescein dye and an argon ion laser to produce a narrow light sheet. Unfortunately, because of the constraints of the Reynolds number range and the requirement for the cylinder diameter to be large enough to provide clear and consistent visualizations, the aspect ratio of the cylinder was only 13.3. This is certainly too small to avoid considerable end effects; however, it was possible to capture some visualizations during the transient time interval prior to the propagation of the contaminating end flow structures towards the central region of the cylinder. Thus the experimental results should only be considered as qualitative, but they still provide a useful comparison with the numerical flow predictions.

Figure 15 shows two comparisons for the steady regimes. The dye visualizations are overlaid with numerically predicted streamlines, which match the observed dye structures reasonably well. Figure 16 shows two comparisons for the unsteady flow. In this case, numerical vorticity fields are used to provide the comparison. Again, the different sets of results show a good match, with the positions and sizes of the near-wake structures in good agreement. It is perhaps surprising that the comparison is so good, given the stability analysis below indicates that the wake undergoes

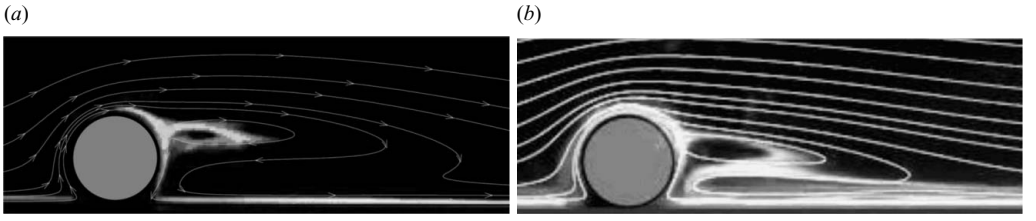

FIGURE 15. A comparison of the streamlines from the numerical simulations with dye visualizations for the steady regime: (*a*) $Re = 100$, $\alpha = -0.5$; (*b*) $Re = 250$, $\alpha = -1$.

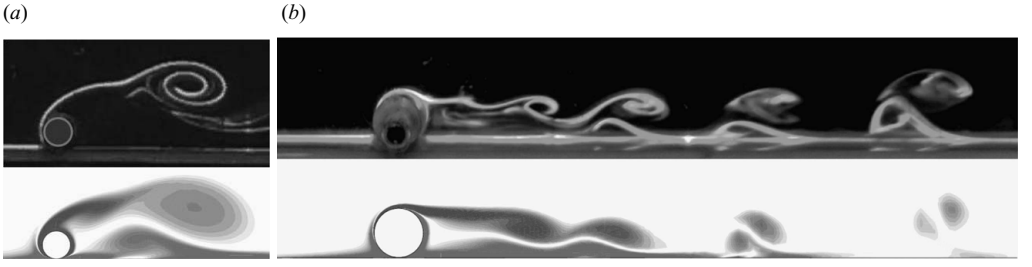

FIGURE 16. A comparison of dye visualizations with numerically predicted vorticity fields for the unsteady regime: (*a*) $Re = 100$, $\alpha = 1$; (*b*) $Re = 450$ (experiments) and $Re = 400$ (numerics) for $\alpha = -1$.

three-dimensional transition well prior to transition to two-dimensional shedding. An interpretation is that the development of three-dimensionality in the flow does not strongly affect the nature of the two-dimensional shedding. In turn, this provides more relevance to the two-dimensional results presented in this section. However, having said this, as indicated above the experimental results show only transient behaviour prior to significant contamination, as the flow cells at the ends of the span grow towards the centre of the cylinder and disrupt the flow there. It is possible that two-dimensional shedding develops faster than the three-dimensional instability and that the contamination by the end cells prevents a different fully saturated three-dimensional time-dependent flow from being seen.

4.4. *St-Re relationship*

In the unsteady regime, the frequency of vortex shedding was measured for each value of α, and the results are shown in figure 17. The Strouhal number increases steadily as α varies from 1 to -1. For all rotation rates apart from $\alpha = -1$, St is lower than for the non-rotating cylinder in an unbounded flow. This is in agreement with the findings of Arnal *et al.* (1991) for the square cylinder sliding along a wall. Arnal *et al.* (1991) also found that St remains fairly constant with changes in Re, and a value of $St \approx 0.08$ was recorded. This is slightly lower than the present value of $St \approx 0.1$ for the circular cylinder with $\alpha = 0$.

The Strouhal number for $\alpha = -0.5$ shows a slight initial decrease with Re. However, this is small in comparison with the variation in St for $\alpha = -1$. In contrast with all the other rotation rates, the shedding frequency for $\alpha = -1$ undergoes a smooth and steady decrease with increasing Re, until an apparent flattening off as $Re \rightarrow 500$. The reason for this difference in the flow is not immediately apparent; it may be due to the greatly reduced vorticity generation at the top of the cylinder in this case, as discussed above. The relative insensitivity of St to Re for a given α (excepting $\alpha = -1$)

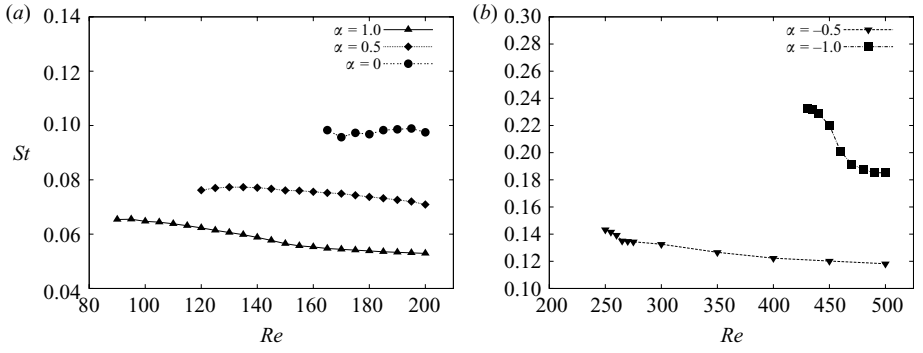

FIGURE 17. Strouhal number plots for all values of α. The trends remain fairly constant over the range of Re considered, except for $\alpha = -1$, where St shows a rapid and steady decrease for $425 < Re < 475$.

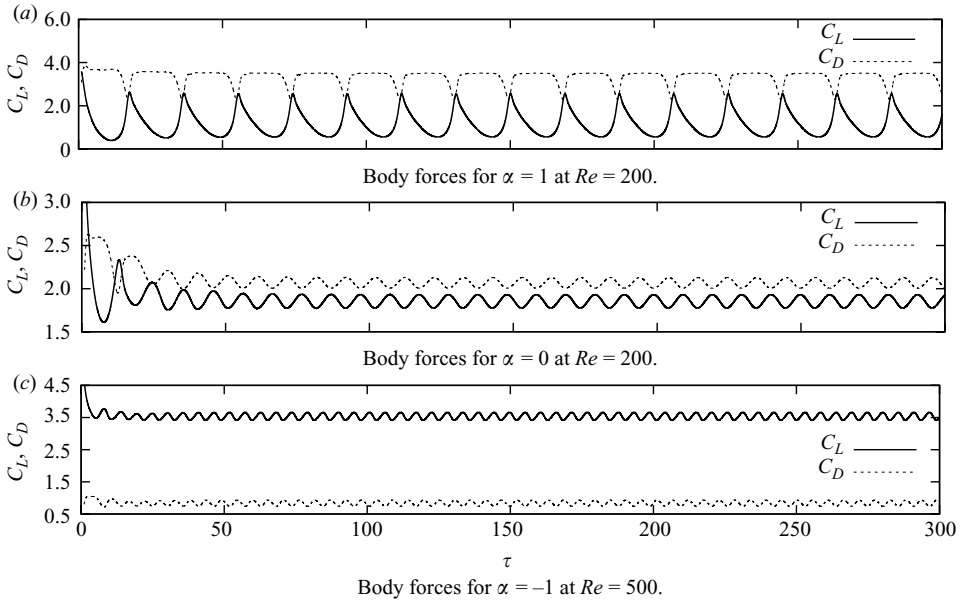

FIGURE 18. Time histories of the unsteady lift and drag coefficients at representative values of the rotation rate.

is in keeping with the results for unsteady flow behind the cylinder near a stationary wall (Arnal *et al.* 1991; Lei *et al.* 1999, 2000; Huang & Sung 2007).

4.5. *Unsteady lift and drag trends*

In the unsteady regime, the force-time histories of the lift and drag forces are given in figure 18. These are shown for the upper Reynolds number limit of the flow studied at representative values of $\alpha = 1$, 0 and -1. Figures 18(*a*)–18(*c*) indicate that the magnitude of fluctuation of the body forces decreases as the rotation rate is varied from forward to reversed rolling, along with the associated increase in shedding frequency mentioned previously.

The perfectly periodic nature of the vortex shedding for the unsteady regime can be characterized by the mean values of the lift and drag, as shown in figures 19 and 20. For $\alpha = 1$, 0.5 and 0, $\bar{C}_D$ and $\bar{C}_L$ show a smooth variation. The mean drag coefficient

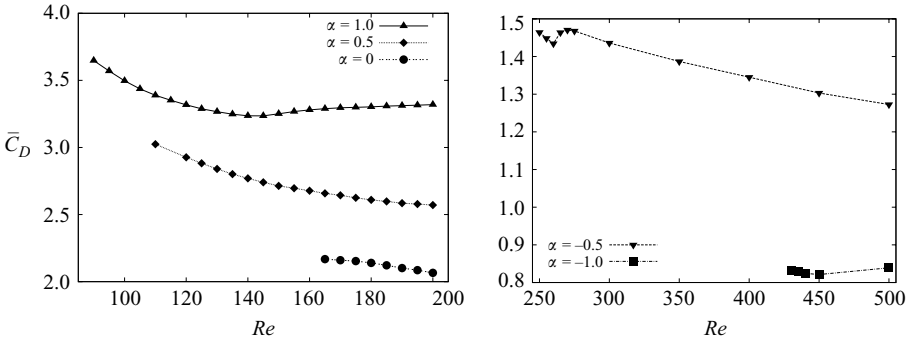

FIGURE 19. Mean values of the drag coefficient during the unsteady regime.

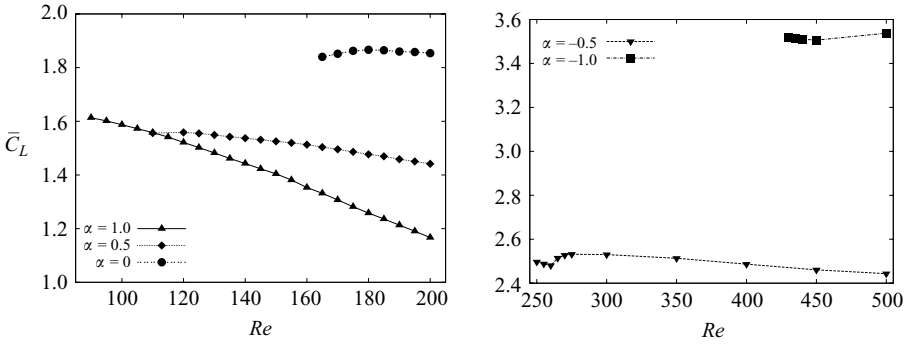

FIGURE 20. Mean values of the lift coefficient for the unsteady regime.

changes greatly with α but has only a weak dependence on Re, with a slight decrease observed as Re increases. The overall value of the drag decreases as α varies from 1 to -1. Meanwhile, the lift steadily decreases for $\alpha = 1$ but is almost constant for $\alpha = 0.5$ and 0. For the negative rotation rates, the lift coefficient is nearly constant but with some variation for Re near the initial onset of unsteady flow. As was the case for the steady flow, the magnitude of $\bar{C}_L$ increases as α goes from 1 to -1, with the greatest increases when $\alpha < 0.5$.

4.6. *Linear stability analysis*

Following the two-dimensional simulations described above, a linear stability analysis was conducted to investigate the stability of the two-dimensional flows to three-dimensional perturbations. The stability of three-dimensional modes was monitored with respect to an associated spanwise wavelength, λ, and the growth rate, σ, recorded. A growth rate greater than zero indicates that the mode will continue to grow over time. For increasing Re, the wavelength at which the growth rate first reaches zero is referred to as the critical wavelength λ_c.

For each of the five values of α investigated, a three-dimensional mode appears at a Reynolds number below the onset of unsteadiness predicted from the two-dimensional simulations. The critical Reynolds number, Re_c, and wavelength as predicted from the linear stability analysis are given in table 2 and also in figure 12 for each value of α. In each instance, the value of Re_c is less than half of the Reynolds number predicted for the development of time-dependent flow in the two-dimensional simulations.

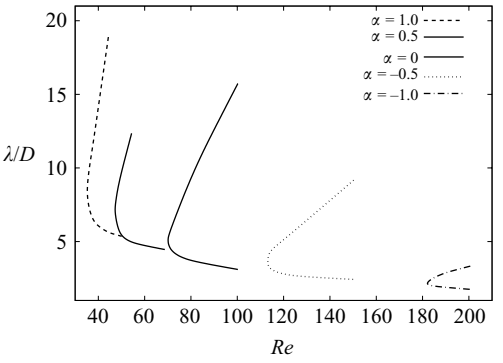

FIGURE 21. Curves of neutral stability for which $\sigma = 0$, indicating the transition to three-dimensional flow.

The three-dimensional mode occurring in the wake of the rolling and sliding cylinder is markedly different from the three-dimensional instabilities occurring behind the cylinder in unbounded flow. For the isolated cylinder, the wake undergoes a Hopf bifurcation while it is still two-dimensional, and the three-dimensional flow develops on the resulting unsteady base flow. In the present study, three-dimensional transition occurs before the two-dimensional flow becomes unsteady, and the critical wavelength varies greatly with α. The large range of λ_c, from $2.2D$ to $8.5D$, indicates that the three-dimensional mode does not scale directly on the fixed physical geometry scale (although presumably it must on the wake geometry).

The fact that the present instability arises on the steady base flow appears more closely associated with a seemingly similar absolute instability in the wake behind a backward-facing step, as reported in the studies by Barkley, Gomes & Henderson (2002) and Beaudoin *et al.* (2004). In their investigation, Barkley *et al.* (2002) found that a backward-facing step with an expansion ratio of 2 undergoes a steady three-dimensional bifurcation at $Re = 748$ (based on the step height H) with a wavelength of approximately $7H$. In their configuration, the downstream wall is stationary with respect to the step, and the wavelength of the instability is directly linked to the length of the recirculation zone. In the study by Beaudoin *et al.* (2004), the critical wavelength varies from $4.5H$ to $7H$ and is dependent, to a certain degree, on the expansion ratio of the channel. A connection between λ_c and the primary recirculation zone is also a possibility in the present study and will be discussed further in § 4.8.

For each value of α, the dominant three-dimensional mode is time invariant, and the numerical code returns converged (to within 0.1 %), real values of the multiplier, $\mu = \sigma T$. From these, and knowing the sampling rate T, the growth rate, σ, is calculated. The values of λ for which $\sigma = 0$ therefore describe the boundaries between the two- and the three-dimensional flow with varying Re. These are often termed contours of neutral stability, and they are plotted for each α in figure 21. For Reynolds numbers to the left of these contours, the flow is steady and two-dimensional, while immediately to right of the curves the flow is steady and three-dimensional. The values of λ_c and Re_c correspond to the leftmost point on each curve.

From the stability analysis, it is possible to plot the fields of perturbation vorticity acting on the two-dimensional, steady base flow. Regions of the flow with a high perturbation vorticity may serve as an indication of the areas in which the instability first develops. Figure 22 shows the contours of streamwise perturbation vorticity at representative values of α. The spanwise vorticity of the two-dimensional base flow

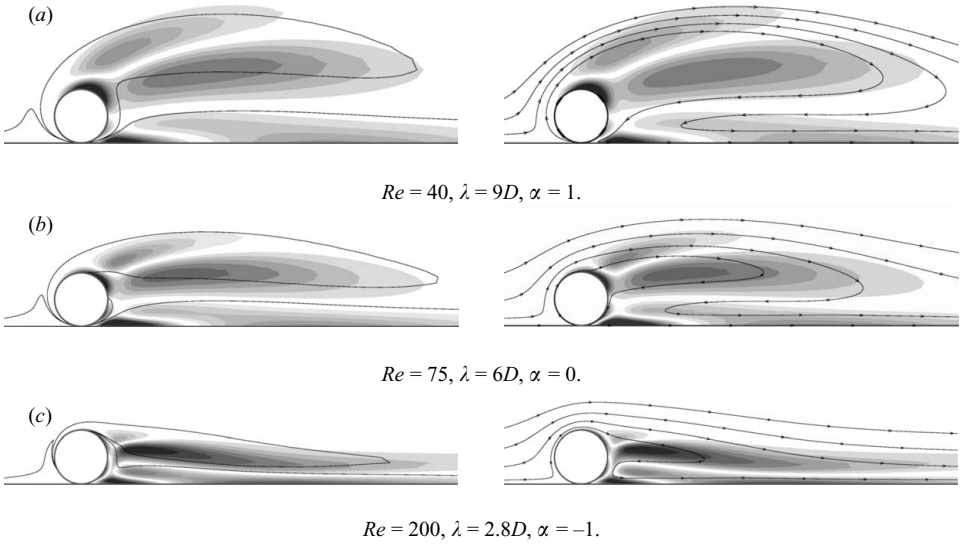

FIGURE 22. Shaded greyscale contour plots of the streamwise perturbation vorticity for various Re-α combinations. The figures to the left are overlaid with the contours of the base flow vorticity, while the figures on the right are overlaid with the streamlines of the base flow. The streamfunction levels have been selected to give an indication of the regions of recirculating flow.

and the streamlines of the flow have also been shown to indicate the structure present in the base flow.

For $\alpha \geqslant 0$, the strongest regions of perturbation vorticity lie on the surface of the cylinder, near the top on the downstream side and on the moving wall just downstream of the cylinder. This configuration has similarities to those reported by Barkley *et al.* (2002) for the backward-facing step, where it was found that the regions of strongest instability (and those with the largest spanwise velocity) occurred on the downstream face of the step and near the reattachment point of the primary recirculation zone. In the present case, there is no concentration of streamwise vorticity at the downstream ends of the upper or lower recirculation zones (the lower recirculation zone was small but present in each of the cases shown in figure 22). Instead, the perturbation vorticity in the wake tends to lie within the limits of the recirculation zones.

The images to the left in figure 22 show areas of streamwise perturbation vorticity associated with the upper region of base flow vorticity. However, it is only for the cases of $\alpha < 0$ that the strength of the vorticity in these regions dominates the perturbation field. In figure 22(c), there remain regions of vorticity on the surface of the cylinder, but these have reduced in both size and magnitude. This is a logical consequence of the reversed rotation of the cylinder, in which the shear at the surface has been significantly reduced.

The perturbation fields obtained from the stability analysis can also be reconstructed as three-dimensional fields, and these are plotted in figure 23. This provides a clearer image of the structure of the perturbation mode and how the sign of vorticity alternates in the spanwise direction. Three-dimensional surface plots of vorticity, illustrating the modes reported in figures 22(a)–22(c), are given in figure 23 over one wavelength of the span. Surfaces of streamwise vorticity are all shown at approximately one quarter of the maximum/minimum. The vortical structures

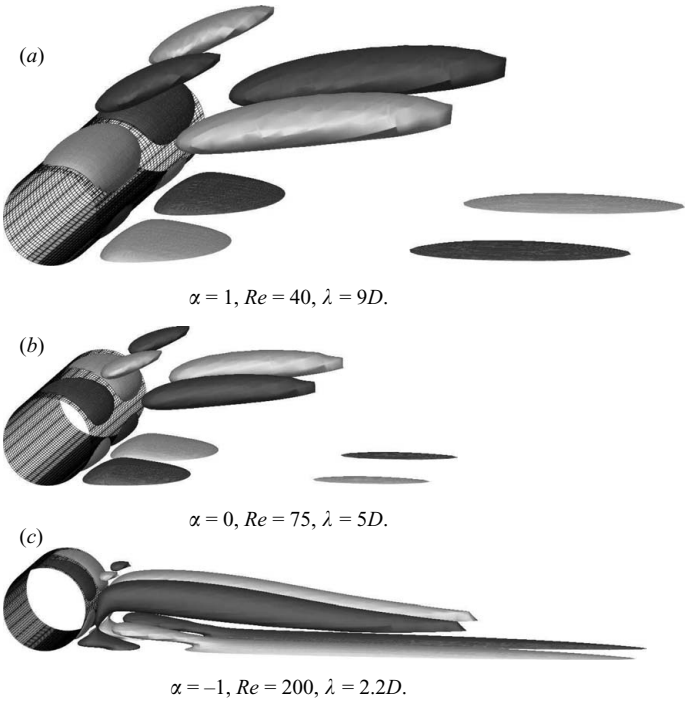

FIGURE 23. Three-dimensional reconstruction of the predicted perturbation mode. Isosurfaces show the streamwise perturbation vorticity.

represent the shape of the dominant linear perturbation mode to the flow. As such, it will not accurately reflect the form of the streamwise vorticity in the fully developed (saturated) three-dimensional flow. After the mode first develops from the initial noise, nonlinearities develop and cause the mode to saturate, thereby resulting in a change to the structure.

As described above for the two-dimensional fields of perturbation vorticity, figure 23 shows the presence of three-dimensional regions of vorticity on the cylinder surface and the downstream wall. The vorticity in the wake takes the form of an opposite-signed pair of flattened streamwise vortices that extend downstream. This is similar to the three-dimensional wake behind the backward-facing step, which is described by Barkley *et al.* (2002) as a series of 'flat rolls'. In the present study, these 'flat rolls' are displaced further from the wall by the relative motion of the wall and the lower recirculation zone. There also exist smaller regions of opposite sign vorticity that lie near the back of the body, away from the wall. These small regions of vorticity are present for $\alpha > 0$ but have almost disappeared when $\alpha = -1$. This suggests that their formation is linked to the size and strength of the vorticity forming on the top surface of the cylinder.

As was the case for the spanwise vorticity observed in the two-dimensional simulations, the placement of the streamwise vortices moves closer to the wall as α varies from 1 to -1. Furthermore, the spanwise length of the structure narrows until, for $\alpha = -1$, the width of each of the streamwise vortices is close to one diameter. In the case of $\alpha = -1$, the perturbation mode looks less like the 'flat rolls' described by Barkley *et al.* (2002) for flow behind the backward-facing step (the form of which

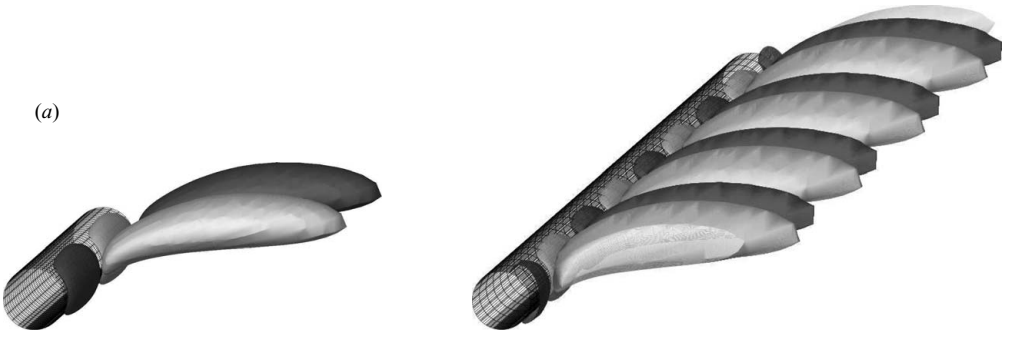

Perturbation mode depicted by transverse vorticity from linear stability analysis (left) and the converged steady field from three-dimensional simulations (right) for $Re = 37$ and $\alpha = 1$.

Same as above except for $Re = 75$ and $\alpha = 0$.

Same as above except for $Re = 190$ and $\alpha = -1$.

FIGURE 24. Comparison between isosurfaces of transverse vorticity from linear analysis and for the fully saturated flow from the three-dimensional simulations. The images on the left show the predicted perturbation mode for the same values of Re and λ as in figure 23. The images on the right show the fully developed wake mode from the three-dimensional simulations, taken over a spanwise distance of 4λ at the Reynolds numbers and rotation rates indicated.

can be seen in figures 23*a* and 23*b*) and more closely resemble Görtler vortices, which form elongated streamwise structures.

4.7. *Three-dimensional simulations*

Direct three-dimensional simulations are used to investigate how the linear modes are modified as the three-dimensional wake develops and saturates. The spanwise domain is set equal to four times the dominant wavelength of the linear instability mode, with 36 Fourier planes used to capture the spanwise variation.

Figure 24 shows the resulting isosurface plots of the transverse vorticity, directed normal to the wall. The images on the left-hand side of figure 24 correspond to the perturbation modes of figure 23, but here, the transverse vorticity has been plotted instead to provide additional information about the structure of the fully developed wake. These isosurfaces are again plotted at one quarter of the maximum/minimum levels and reflect the swirling motion of the fluid in a plane parallel to the moving wall. The three-dimensional simulations show a distance of 4λ in the spanwise direction. Note that the transverse vorticity is zero for the two-dimensional flow. These results provide a qualitative comparison between the predicted and observed

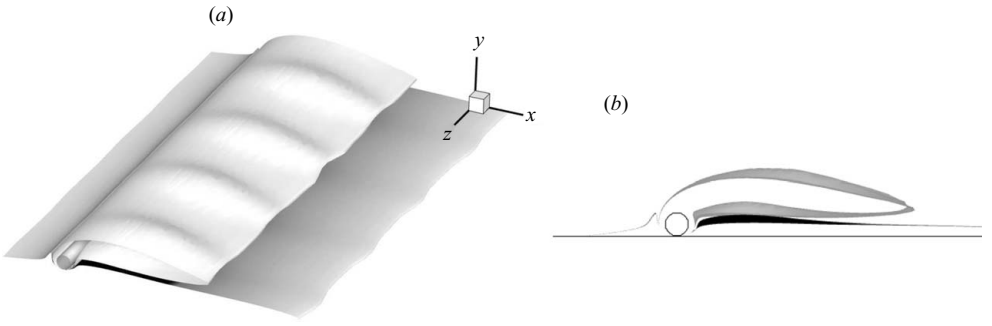

FIGURE 25. Isosurface plots of spanwise vorticity ($\omega_z = \pm 0.5$) from a three-dimensional simulation at $Re = 40$ and $\alpha = 1$: (*a*) perspective view; (*b*) side view showing the projected extent of the waviness.

vortical structures in the wake, showing that a very good agreement exists between the two. This indicates that the fully saturated instability mode is in fact only slightly modified from the predicted linear mode. This is somewhat of a reflection that the transition is supercritical and that the Reynolds number is close to the critical value.

Perhaps an important point is that the transition to three-dimensional flow does not strongly change the underlying two-dimensional structure of the wake. For example, figure 25 shows isosurfaces of 'spanwise' vorticity for $Re = 40$ and $\alpha = 1$ from three-dimensional simulations. This shows that the development of wake three-dimensionality only causes the otherwise two-dimensional vorticity isosurfaces to become wavy. The minimal distortion from the two-dimensional state is highlighted by the right-hand-side image, which shows an end-on view of the same isosurfaces.

An interesting observation is that the three-dimensional simulations only displayed a converged, steady three-dimensional flow for a small range of Reynolds numbers above the predicted transition (within approximately 5 % of Re_c). Beyond this range of Re, after the initial development of the three-dimensional mode, the spanwise velocity in the wake showed a small magnitude oscillation that grew slowly over time. For example, for both $\alpha = 1$ and -1, unsteadiness is present in the wake for $Re = 40$ and 200, respectively, only slightly above the critical values of $Re_c = 35.6$ and 182. However, this unsteadiness is of such a low magnitude that it does not reflect any marked change to the wake structure with time. From the results of the three-dimensional simulations, it therefore appears that at Reynolds numbers only slightly in excess of the critical values, the development and initial saturation of steady three-dimensional flow causes a further subsequent transition to unsteady flow. This is unrelated to the steady-to-unsteady transition for the numerically imposed two-dimensional flow, which occurs at considerably higher Reynolds numbers.

4.8. *The transition mechanism*

The mechanism responsible for the transition to three-dimensional steady flow is not immediately apparent. Given that the three-dimensional flow bears similarities to the wake reported behind the backward-facing step, this was used as a starting point for identifying the mechanism. Some debate remains regarding the transition mechanism for the backward-facing step flow; however, evidence suggests some type of centrifugal instability. One explanation is put forward by Ghia, Osswald & Ghia (1989) who proposed that Taylor–Görtler vortices form as the result of the concave shear layer passing over the top of the step, between the upper and lower recirculation

zones. Barkley *et al.* (2002) discounted this theory, stating that they found the region of concave flow to remain linearly stable over a large range of Re and that the instability does not take the form of streamwise vortices in the main flow, as would be expected, but is linked to the primary recirculation zone behind the step.

A connection between the three-dimensional instability and the location of the lower recirculation zone is noted in the present study. Even for the case of $\alpha = -1$ (figure 23*c*), when the streamwise vortices are less flattened, the structures are confined to the regions of recirculating fluid. From their stability analysis of the backward-facing step, Barkley *et al.* (2002) believed the mechanism of transition to be centrifugal in nature, and they associated it with the closed streamlines in the primary recirculation zone. A method similar to that used by Barkley *et al.* (2002) has therefore been employed to analyse the steady two-dimensional recirculating flow for possible regions of instability.

At this point, it is worth mentioning that the onset of the three-dimensional flow, as predicted by the stability analysis, occurs very close to the Reynolds number at which the lower recirculation zone is first observed in the two-dimensional simulations for $\alpha = 1$, 0.5 and 0. It is therefore possible that the formation of this recirculation zone plays a part in the onset of three-dimensional flow. For this reason, both the upper and lower recirculation zones are tested for regions of centrifugal instability.

The basic premise for centrifugal instability is Rayleigh's criterion (as outlined in Drazin & Reid 1981), and this was generalized by Bayly (1988) for the case of inviscid flow with convex closed streamlines. Bayly (1988) stated that regions of possible centrifugal instability arise when the streamlines are closed (as in a zone of recirculating fluid) and that the circulation decreases outwards in some portion of the flow. This condition is satisfied in the flow behind a blockage or backward-facing step (Barkley *et al.* 2002; Griffith *et al.* 2007), when the presence of the stationary walls reduces the velocity of the nearby flow to such an extent that the overall circulation is reduced. For the backward-facing step, Barkley *et al.* (2002) found these conditions to be satisfied on the wall immediately downstream of the step and at the reattachment point of the limiting streamline representing the primary recirculation zone.

Given the above requirements for centrifugal instability, and the fact that the circulation Γ is defined as the integral of $\boldsymbol{u} \cdot d\boldsymbol{l}$ (where $\boldsymbol{u}$ is the velocity and $d\boldsymbol{l}$ an incremental length) around one circuit of the streamline, it is possible within the numerical code to calculate a value of Γ for a series of streamlines within each recirculation zone. The above process was carried out for both recirculation zones at $\alpha = 1$, $Re = 50$, $\alpha = 0$, $Re = 75$ and $\alpha = -1$, $Re = 300$ on the two-dimensional flow. For all these α-Re pairs, the flow is three-dimensional, and both recirculation zones are fully formed. However, no evidence of outwardly decreasing circulation was found in any of the above cases. This does not eliminate the possibility of a centrifugal instability in the flow but suggests that if one is present, it does not originate within the highly elliptical recirculation zones. With consideration, the lack of a decrease in circulation can be clearly accounted for by the presence of the moving wall. In the present study, where the frame of reference is attached to the cylinder centre, there are no stationary boundaries (except for the cylinder surface when $\alpha = 0$) to cause a decrease in the velocity of the flow. Rather, the motion of the recirculating fluid in each case is accelerated by the moving boundaries, causing an increase in $\boldsymbol{u}$ and Γ.

Given the recent work by Griffith *et al.* (2007), it is possible that the physical mechanism mainly responsible for the transition is an elliptic instability of the recirculation zone. This instability occurs in flows with elliptic streamlines such as the flow associated with a vortex in an external strain field. The interaction of the

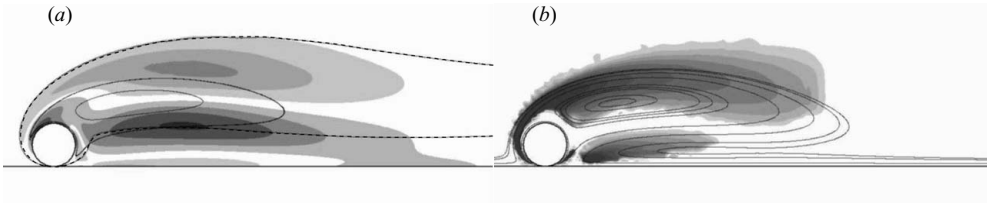

FIGURE 26. (*a*) Spanwise perturbation vorticity for $\alpha = 1$, $Re = 40$. The streamlines are overlaid. The dashed line corresponds to $\omega = -0.2D/U$, indicating the position of the upper attached vortex. (*b*) Contours of inviscid growth rate assuming local elliptic instability. Again, the streamlines are overlaid to show the location of the recirculation zone.

strain with the normally neutral perturbation modes of the vortex leads to resonant amplification, resulting in three-dimensional deformation of the vortex core. The general theory can be found in Kerswell (2002). Support for this point of view is provided by figure 26. Figure 26(*a*) shows the spanwise perturbation vorticity for $\alpha = 1$ and $Re = 40$ (one of the cases considered in figure 22). The streamlines are overlaid. These indicate that the zero contour passes almost through the centre of the recirculation with the instability lobes on either side. This is also observed for the other rotation rates. Interestingly, the lobes are contained within the attached clockwise vortical region as would be expected for an elliptic instability. For an idealized elliptic instability the alignment is at 45° to the ellipse axes, and the instability is contained within the vortex; however, the situation here is somewhat distant from the idealized case, which would allow a rigorous analytic treatment. In that case the inviscid growth rate is approximately given by

$$\sigma_i = \frac{9\epsilon}{16}(1 - \beta^m)^n,$$

where ϵ is the strain rate and m and n are constants given by $m = 2.811$ and $n = 0.3914$ (see Landman & Saffman 1987; Leweke & Williamson 1998). Here, $\beta = 2\epsilon/\omega$, which is constant for the idealized case, with ω the spanwise vorticity. If these relationships are assumed to apply locally, an inviscid growth rate can be determined as a function of space. This is shown in figure 26(*b*). A considerable part of the recirculation zone shows a positive growth rate, including near the centre of the recirculation. This provides support for the hypothesis that the essential mechanism supporting the growth of the three-dimensional mode is elliptic. For finite-sized vortices, the preferred spanwise wavelength depends on the core size. For a strained Gaussian vortex, Le Dizes & Laporte (2002) showed that this spanwise wavelength is given by $\lambda/a = 2.78$, where a is the Gaussian length scale. For a highly strained elliptical vortex the appropriate length scale can be extracted from the axis lengths of the ellipse and is given by $a^2 = (a_M^2 + a_m^2)/2$, where a_M and a_m are the semi-major and semi-minor axis lengths, respectively (Le Dizes & Verga 2002).

For the cases shown in figure 22 the spanwise vorticity perturbation field is restricted to the vortical region. The vertical sizes of the upper vortical regions are very approximately $2.2D$, $1.5D$ and $0.75D$, for $\alpha = 1$, 0 and -1, respectively. This is just the vertical distance between the dashed contours in figure 22. In each case, the ratio of the axis lengths of the elliptical streamlines close to the centre of the recirculation zone is close to 5:1. Given that in the slightly strained case, the diameter of the region delimited by the approximately circular zero-amplitude contour for the perturbation field is about $1.7a$, these numbers suggest the preferred wavelengths for

the three cases of approximately $13D$, $8.8D$ and $4.4D$. These are about 50 % greater than the observed preferred wavelengths at these Reynolds numbers of $9D$, $6D$ and $2.8D$; however, given the assumptions and approximations involved, this is perhaps a surprisingly good match.

For a flow through constricted channels showing similar spanwise perturbation vorticity and inviscid growth rate distributions, Griffith *et al.* (2007) showed that the onset of the instability is consistent with the elliptic mechanism given the observed preferred wavelengths; i.e. the viscous damping and inviscid elliptic growth balance at approximately the correct transition Reynolds numbers. Perhaps it is also of note that for that case it was shown that the centrifugal mechanism does not provide positive growth rates, and in any case for a centrifugal instability the most unstable wavelengths are far from those predicted from instability analysis and three-dimensional simulations. Thus, it appears that the elliptic mechanism is much more likely to be a contributor to the three-dimensional transition for this flow.

5. Conclusions

The numerical simulations have shown that in the small gap region present between the cylinder and the wall, the flow experiences a strong reversal in direction on both the upstream and the downstream side of the cylinder. The flow in this near-contact region is characterized by either one or two stagnation points, and the location and number of these points depends on the rotation rate of the cylinder. In the steady flow regime, two recirculation zones are observed in the wake behind the cylinder, and these grow linearly with Re, as is reported for the steady wake behind a cylinder in an unbounded flow (Taneda 1956; Kawaguti 1966; Tamaki & Keller 1969; Dennis & Chang 1970).

When the Reynolds number is increased in the steady regime, the lift and drag forces on the cylinder both decrease. For $\alpha > 0$, the drag dominates the system, while negative rotation rates vary from being drag dominated to being lift dominated with increasing Re in the steady flow regime. This trend was similar to that observed by Cheng & Luo (2007) for the rotating cylinder near a stationary wall.

Larger magnitude, negative rotation rates are shown to provide the most stable flow, with the unsteady transition delayed until higher Reynolds numbers. The values of $\alpha > 0$ act to destabilize the flow and decrease the Reynolds number of transition, while $\alpha < 0$ creates a more stable flow that delays the transition. The unsteady flow resulting from the two-dimensional simulations has similarities to that which develops behind a cylinder in a free stream, with opposite-signed vortices forming a pair in the wake. However, in the case of the cylinder near the wall, one vortex is formed from the shear layer over the top of the cylinder, and an opposite-signed vortex is induced in the wall shear layer behind the body. These vortex pairs propel away from the wall as they move downstream.

From the linear stability analysis, it was discovered that the wake behind the rolling cylinder undergoes a transition to steady three-dimensional flow, prior to the onset of unsteady flow. This has similarities to the flow behind a backward-facing step, but no clear link has been established between the mechanism governing these two transitions. The spanwise wavelength of the three-dimensional mode is strongly dependent on the rotation rate of the cylinder, and the structure of this time invariant perturbation mode is verified with the use of three-dimensional simulations. For several of the rotation rates studied, the three-dimensional mode first appears at the same Reynolds number as the lower recirculation zone in the two-dimensional

simulations. This may be a coincidence, but some opportunity for further study presents itself. Results of the three-dimensional simulations indicate that the saturated three-dimensional mode remains steady only for a small range of Reynolds numbers above the predicted transition. It appears that the three-dimensionality triggers the early onset of unsteadiness in the wake.

It was considered whether it was possible that the three-dimensional mode develops as the result of a centrifugal instability in the flow. Towards this end, calculations were carried out on the closed streamlines of the upper and lower recirculation zones to determine if Rayleigh's criterion was satisfied. However, the circulation was found to be always outwardly increasing, and the findings indicate that a centrifugal instability does not develop within the recirculation zones. A further analysis was then conducted into whether an elliptic instability of the recirculation zones could be responsible. The observed distribution of spanwise perturbation vorticity within the recirculation zone, the observed wavelengths and the determination that the inviscid growth rate was strongly positive over large areas of the recirculation zone support this hypothesis. In addition, an analogy of the present flow with a related flow past semicircular blockages within a channel, in which the elliptic analysis was extended slightly further, provide further support for this conclusion.

The support from Australian Research Council Discovery Grants DP0877327 and DP0877517 and computing time from the Australian Partnership for Advanced Computing are gratefully acknowledged. Bronwyn Stewart would also like to acknowledge the support of a Monash University Postgraduate Publication Award in making this research possible.

REFERENCES

Armaly, B. F., Durst, F., Pereira, J. C. F. & Schönung, B. 1983 Experimental and theoretical investigation of backward-facing step flow. *J. Fluid Mech.* **127**, 473–496.

Arnal, M. P., Goering, D. J. & Humphrey, J. A. C. 1991 Vortex shedding from a bluff body adjacent to a plane sliding wall. *Trans. ASME: J. Fluids Engng* **113**, 384–398.

Barkley, D., Gomes, M. G. M. & Henderson, R. D. 2002 Three-dimensional instability in flow over a backward-facing step. *J. Fluid Mech.* **473**, 167–190.

Barkley, D. & Henderson, R. D. 1996 Three-dimensional Floquet stability analysis of the wake of a circular cylinder. *J. Fluid Mech.* **322**, 215–241.

Barkley, D., Tuckerman, L. S. & Golubitsky, M. 2000 Bifurcation theory for three-dimensional flow in the wake of a circular cylinder. *Phys. Rev.* E **61** (5), 5247–5252.

Barnes, F. H. 2000 Vortex shedding in the wake of a rotating circular cylinder at low Reynolds numbers. *J. Phys.* D **33**, L141–L144.

Bayly, B. J. 1988 Three-dimensional centrifugal-type instabilities in inviscid two-dimensional flows. *Phys. Fluids* **31** (1), 56–64.

Bearman, P. W. & Zdravkovich, M. M. 1978 Flow around a circular cylinder near a plane boundary. *J. Fluid Mech.* **89**, 33–47.

Beaudoin, J.-F., Cadot, O., Aider, J.-L. & Wesfreid, J. E. 2004 Three-dimensional stationary flow over a backward-facing step. *Eur. J. Mech* B **23**, 147–155.

Chen, Y.-M., Ou, Y.-R. & Pearlstein, A. J. 1993 Development of the wake behind a circular cylinder impulsively started into a rotatory and rectilinear motion. *J. Fluid Mech.* **253**, 449–484.

Cheng, M. & Luo, L.-S. 2007 Characteristics of two-dimensional flow around a rotating circular cylinder near a plane wall. *Phys. Fluids* **19**, 063601-1–063601-17.

Chorin, A. J. 1968 Numerical solution of the Navier–Stokes equations. *Math. Comput.* **22**, 745–762.

Dennis, S. C. R. & Chang, G.-Z. 1970 Numerical solutions for steady flow past a circular cylinder at Reynolds numbers up to 100. *J. Fluid Mech.* **42**, 471–489.

Díaz, F., Gavaldà, J., Kawakk, J. G., Keffer, J. F. & Giralt, F. 1983 Vortex shedding from a spinning cylinder. *Phys. Fluids* **26** (12), 3454–3460.

Dipankar, A. & Sengupta, T. K. 2005 Flow past a circular cylinder in the vicinity of a plane wall. *J. Fluids Struct.* **20** (3), 403–423.

Drazin, P. G. & Reid, W. H. 1981 *Hydrodynamic Stability*. Cambridge University Press.

Fornberg, B. 1985 Steady viscous flow past a circular cylinder up to Reynolds number 600. *J. Comput. Phys.* **61**, 297–320.

Ghia, K. N., Osswald, G. A. & Ghia, U. 1989 Analysis of incompressible massively separated viscous flows using unsteady Navier–Stokes equations. *Intl J. Numer. Methods Fluids* **9**, 1025–1050.

Griffith, M. D., Thompson, M. C., Leweke, T., Hourigan, K. & Anderson, W. P. 2007 Wake behaviour and instability of flow through a partially blocked channel. *J. Fluid Mech.* **582**, 319–340.

Henderson, R. D. 1997 Nonlinear dynamics and pattern formation in turbulent wake transition. *J. Fluid Mech.* **352**, 65–112.

Huang, W.-X. & Sung, H. J. 2007 Vortex shedding from a circular cylinder near a moving wall. *J. Fluids Struct.* **23**, 1064–1076.

Ingham, D. B. 1983 Steady flow past a rotating cylinder. *Comp. Fluids* **11** (4), 351–366.

Jackson, C. P. 1987 A finite-element study of the onset of vortex shedding in the flow past variously shaped bodies. *J. Fluid Mech.* **182**, 23–45.

Jaminet, J. F. & Van Atta, C. W. 1969 Experiments on vortex shedding from rotating circular cylinders. *AIAA J.* **7**, 1817–1819.

Kang, S., Choi, H. & Lee, S. 1999 Laminar flow past a rotating circular cylinder. *Phys. Fluids* **11** (11), 3312–3321.

Kano, I. & Yagita, M. 2002 Flow around a rotating circular cylinder near a moving plane wall. *Japanese Soc. Mech. Eng. Intl J* B **45** (2), 259–268.

Karniadakis, G. E., Israeli, M. & Orszag, S. A. 1991 High-order splitting methods for the incompressible Navier–Stokes equations. *J. Comput. Phys.* **97**, 414–443.

Kawaguti, M. 1966 Numerical study of a viscous fluid flow past a circular cylinder. *J. Phys. Soc. Jpn* **21** (10), 2055–2062.

Kerswell, R. R. 2002 Elliptical instability. *Annu. Rev. Fluid Mech.* **34**, 83–113.

Landman, M. J. & Saffman, P. G. 1987 The three-dimensional instability of strained vortices in a viscous fluid. *Phys. Fluids* **30**, 2339–2342.

Le Dizes, S. & Laporte, F. 2002 Theoretical predictions for the elliptic instability in a two-vortex flow. *J. Fluid Mech.* **471**, 169–201.

Le Dizes, S. & Verga, A. 2002 Viscous interaction of two co-rotating vortices before merging. *J. Fluid Mech.* **467**, 389–410.

Lei, C., Cheng, L., Armfield, S. W. & Kavanagh, K. 2000 Vortex shedding suppression for flow over a circular cylinder near a plane boundary. *Ocean Engng* **27**, 1109–1127.

Lei, C., Cheng, L. & Kavanagh, K. 1999 Re-examination of the effect of a plane boundary on force and vortex shedding of a circular cylinder. *J. Wind Engng Indus. Aerodyn.* **80**, 263–286.

Leontini, J. S., Thompson, M. C. & Hourigan, K. 2007 Three-dimensional transition in the wake of a transversely oscillating cylinder. *J. Fluid Mech.* **577**, 79–104.

Leweke, T. & Williamson, C. H. K. 1998 Three-dimensional instabilities in wake transition. *Eur. J. Mech.* B **17** (4), 571–586.

Lim, T. T., Sengupta, T. K. & Chattopadhyay, M. 2004 A visual study of vortex-induced subcritical instability on a flat plate boundary layer. *Exp. Fluids* **37**, 47–55.

Mittal, S. & Kumar, B. 2003 Flow past a rotating cylinder. *J. Fluid Mech.* **476**, 303–334.

Nishino, T., Roberts, G. T. & Zhang, X. 2007 Vortex shedding from a circular cylinder near a moving ground. *Phys. Fluids* **19**, 025103-1–025103-12.

Provansal, M., Mathis, C. & Boyer, L. 1987 Benard–von Kármán instability: transient and forced regimes. *J. Fluid Mech.* **182**, 1–22.

Roshko, A. 1954 On the development of turbulent wakes from vortex streets. *Tech Rep.* 1191. National Advisory Committee for Aeronautics.

Ryan, K., Thompson, M. C. & Hourigan, K. 2005 Three-dimensional transition in the wake of bluff elongated cylinders. *J. Fluid Mech.* **538**, 1–29.

Seddon, J. R. T. & Mullin, T. 2006 Reverse rotation of a cylinder near a wall. *Phys. Fluids* **18**, 041703-1–041703-4.

Sengupta, T. K., De, S. & Sarkar, S. 2003 Vortex-induced instability of an incompressible wall-bounded shear layer. *J. Fluid Mech.* **493**, 277–286.

Sheard, G. J., Thompson, M. C. & Hourigan, K. 2003 From spheres to circular cylinders: the stability and flow structures of bluff ring wakes. *J. Fluid Mech.* **492**, 147–180.

Stewart, B. E., Leweke, T., Hourigan, K. & Thompson, M. C. 2008 Wake formation behind a rolling sphere. *Phys. Fluids* **20**, 071704-1–071704-4.

Stewart, B. E., Thompson, M. C., Leweke, T. & Hourigan, K. 2009 Numerical and experimental studies of the rolling sphere wake. *J. Fluid Mech.* . Forthcoming.

Tamaki, H. & Keller, H. B. 1969 Steady two-dimensional viscous flowof an incompressible fluid past a circular cylinder. *Phys. Fluids Suppl. II* **12** (12), II-51–II-56.

Taneda, S. 1956 Experimental investigation of the wakes behind cylinders and plates at low Reynolds numbers. *J. Phys. Soc. Jpn* **11** (3), 302–307.

Taneda, S. 1965 Experimental investigation of vortex streets. *J. Phys. Soc. Jpn* **20** (9), 1714–1721.

Tang, T. & Ingham, D. B. 1991 On steady flow past a rotating circular cylinder at Reynolds numbers 60 and 100. *Comp. Fluids* **19** (2), 217–230.

Thompson, M. C., Hourigan, K., Cheung, A. & Leweke, T. 2006 Hydrodynamics of a particle impact on a wall. *Appl. Math. Model.* **30**, 1356–1369.

Thompson, M. C., Leweke, T. & Provansal, M. 2001*a* Kinematics and dynamics of sphere wake transition. *J. Fluids and Struct.* **15**, 575–585.

Thompson, M. C., Leweke, T. & Williamson, C. H. 2001*b* The physical mechanism of transition in bluff body wakes. *J. Fluids Struct.* **15**, 607–616.

Van Atta, C. W. 1997 Comments on 'Hopf bifurcation in wakes behind a rotating and translating circular cylinder'. *Phys. Fluids* **9** (10), 3105–3106.

Williamson, C. 1996 Three-dimensional wake transition. *J. Fluid Mech.* **328**, 345–407.

Williamson, C. H. K. 1988 The existence of two stages in the transition to three-dimensionality of a cylinder wake. *Phys. Fluids* **31** (11), 3165–3168.

Zdravkovich, M. M. 1985 Forces on a circular cylinder near a plane wall. *Appl. Ocean Res.* **7** (4), 197–201.